Eur. Phys. J. C (2020) 80:908
https://doi.org/10.1140/epjc/s10052-020-08480-z

THE EUROPEAN PHYSICAL JOURNAL C

Regular Article - Theoretical Physics

Phenomenology of scotogenic scalar dark matter

Ivania M. Ávila[1,2,a], **Valentina De Romeri**[2,b], **Laura Duarte**[2,3,c], **José W. F. Valle**[2,d]

[1] Instituto de Física, Pontificia Universidad Católica de Chile, Av. Vicuña Mackenna, 4860 Santiago de Chile, Chile
[2] AHEP Group, Institut de Física Corpuscular, CSIC/Universitat de València, Parc Científic de Paterna, C/ Catedrático José Beltrán, 2, 46980 Paterna, Valencia, Spain
[3] Departamento de Física e Química, Universidade Estadual Paulista (UNESP), Guaratinguetá, SP, Brazil

Received: 25 February 2020 / Accepted: 16 September 2020 / Published online: 1 October 2020
© The Author(s) 2020

Abstract We reexamine the minimal Singlet + Triplet Scotogenic Model, where dark matter is the mediator of neutrino mass generation. We assume it to be a scalar WIMP, whose stability follows from the same $\mathbb{Z}_2$ symmetry that leads to the radiative origin of neutrino masses. The scheme is the minimal one that allows for solar and atmospheric mass scales to be generated. We perform a full numerical analysis of the signatures expected at dark matter as well as collider experiments. We identify parameter regions where dark matter predictions agree with theoretical and experimental constraints, such as neutrino oscillations, Higgs data, dark matter relic abundance and direct detection searches. We also present forecasts for near future direct and indirect detection experiments. These will further probe the parameter space. Finally, we explore collider signatures associated with the mono-jet channel at the LHC, highlighting the existence of a viable light dark matter mass range.

1 Introduction

After the discovery of the Higgs boson, the particle physics community is eager to discover new phenomena, that would imply physics beyond the Standard Model (SM). Together with the evidence for dark matter, neutrino physics remains as the most solid indication of new physics. Neutrino experiments point towards two different neutrino mass squared differences, associated to solar and atmospheric oscillations. Hence, at least two of the three active neutrino species must be massive. Here we adopt the minimal picture in which one of the neutrinos is (nearly) massless. This is achieved in "missing partner" seesaw mechanisms [1] where one of the "left-handed" neutrinos fails to pair-off.[1] The presence of a massless neutrino has a very simple and clear implication concerning neutrinoless double beta ($0\nu2\beta$) decay.

Indeed, if the lightest neutrino is massless, there is only one physical Majorana phase, and the effective mass parameter characterizing the amplitude for $0\nu2\beta$ decay has a lower limit, even for a normal neutrino mass ordering, as currently preferred by oscillation data [3,4]. This is in sharp contrast to the standard three-massive-neutrino-scenario in which there can be in general a destructive interference amongst the three light neutrinos (such cancellation in $0\nu2\beta$ decay may also be avoided in the three-massive-neutrino case in the presence of specific family symmetries [5–7]).

Our minimal scenario is a generalization of the scotogenic model initially proposed in [8]. The basic idea of this approach is that dark matter is the mediator of neutrino mass generation, and that the same $\mathbb{Z}_2$ symmetry that makes the neutrino mass to have radiative origin also serves to stabilize dark matter. We reexamine the Singlet + Triplet Scotogenic Model extension proposed in [9], which generalizes the original idea introduced in [8], making its phenomenology viable and substantially richer. The presence of Singlet and Triplet fermions in such a scotogenic model extension automatically leads to two oscillation lengths associated to solar and atmospheric oscillations, that can be traced to each of the dark fermion types, leaving a massless neutrino. Compared to the simple scotogenic model, the unwanted spontaneous breaking of the $\mathbb{Z}_2$ parity symmetry [10] can be naturally avoided due to the effect of the new couplings, as discussed in [11]. Two dark matter candidates can be envisaged within the scotogenic framework, either the lightest dark fermion or the isodoublet dark scalar boson. Either possibility corresponds to that of a weakly interacting massive particle (WIMP), produced thermally in the early Universe, similarly to the SM

[a] e-mail: idmaturana@uc.cl
[b] e-mail: deromeri@ific.uv.es (corresponding author)
[c] e-mail: l.duarte@unesp.br
[d] e-mail: valle@ific.uv.es

[1] Hybrid schemes with just one seesaw-neutrino-mass and one radiative-mass can also describe neutrino oscillations [2].

particles. Either will constitute what is called cold dark matter.

Following [12] here we focus on the case of scalar WIMP dark matter. The fermionic dark matter case mimics neutralino dark matter in supersymmetry [9] and has been recently re-visited in Refs. [13–15]. As we will see, scalar WIMP dark matter phenomenology in the Singlet + Triplet Scotogenic Model provides a rich scenario, sharing common features with other dark matter models such as the Inert Higgs Doublet Model [16–20] and with discrete dark matter models [21,22]. In this paper we build upon previous analyses, expanding them by including a more detailed phenomenological study of the scalar dark matter candidate. From the dark matter point of view our work contains many new improvements. The updated experimental constraints, in particular from dark matter direct detection experiments like XENON-1T, cut out a relevant region of the parameter space especially in the mass range around and above 100 GeV. Then we present a novel analysis of indirect probes via γ rays. Here we compare both current as well as future γ-ray telescopes. Finally, we perform a new collider study focusing on the $\not{E}_T$ + jet (mono-jet) signal, with relevant implications for future Large Hadron Collider (LHC) searches with higher luminosity. Moreover, we stress an interesting feature of this scenario for neutrinoless double beta decay facilities, namely the existence of a lower bound that holds even for normal neutrino mass ordering. This is very promising for the upcoming experiments. While this feature is generic to any theory in which one of the light neutrinos is massless, we stress that it comes automatically in this model, allowing for a testable connection between neutrino physics and dark matter.

The paper is organised as follows. In Sect. 2 we introduce the model, detailing the new fields and new interactions present. We describe in detail the scalar and fermionic sector, as well as the radiative neutrino mass generation, emphasizing that the lightest neutrino is massless and discussing the resulting lower bound for neutrinoless double beta decay.

Section 3 describes the numerical analysis used to study the dark matter sector of the model, listing the main constraints included. Here we have assumed that the dark matter is a scalar particle. In Sect. 4 we present the main results concerning the relic scalar dark matter density, direct and indirect detection. In Sect. 5 we deal with the implications for the LHC searches, taking into account the main results of the previous section. We focus on the $\not{E}_T$ + jet (mono-jet) signal. Finally, we give our conclusions in Sect. 6.

2 The Singlet + Triplet scotogenic model

In this section we will review the Singlet + Triplet Scotogenic Model. This generalization of the scotogenic model [8] was proposed in [9] and further studied in several papers [11–14]. In addition to the SM gauge symmetry there is a discrete $\mathbb{Z}_2$ symmetry, whose role is to make the lightest $\mathbb{Z}_2$-odd or "dark" particle stable and to ensure the radiative generation of neutrino masses. The SM particle content is augmented by the inclusion of a Majorana fermion triplet Σ and a Majorana fermion singlet F, both odd under the $\mathbb{Z}_2$ symmetry. Moreover, the model includes a new scalar doublet η – odd under the $\mathbb{Z}_2$ symmetry, which does not acquire a vacuum expectation value (VEV) – and a triplet scalar Ω, which allows for the mixing of the neutral parts of the new fermions. This triplet scalar field has a zero hypercharge and it is even under the $\mathbb{Z}_2$ symmetry, thus, its neutral component can acquire a nonzero VEV. The full particle content of the model is given in Table 1, with the corresponding charge assignment under the different symmetry groups.

Table 1 Particle content and quantum numbers of the Singlet + Triplet Scotogenic Model. The charge assignments of the fields under the global Lepton Number symmetry (L) are also shown

Generations	Standard model			New fermions		New scalars	
	L	e	ϕ	Σ	F	η	Ω
	3	3	1	1	1	1	1
$SU(3)_C$	1	1	1	1	1	1	1
$SU(2)_L$	2	1	2	3	1	2	3
$U(1)_Y$	-1	-2	1	0	0	1	0
$\mathbb{Z}_2$	$+$	$+$	$+$	$-$	$-$	$-$	$+$
L	1	1	0	0	0	-1	0

Taking into account the new fields and symmetries of the model, the relevant terms of the Lagrangian read

$$\begin{aligned}\mathcal{L} \subset & -Y^{\alpha\beta} L_\alpha e_\beta \phi - Y_F^\alpha (\bar{L}_\alpha \tilde{\eta}) F - Y_\Sigma^\alpha \bar{L}_\alpha^c \Sigma^\dagger \tilde{\eta} \\ & - Y_\Omega \mathrm{Tr}[\bar{\Sigma}\Omega] F \\ & - \frac{1}{2} M_\Sigma \mathrm{Tr}(\overline{\Sigma}^c \Sigma) - \frac{M_F}{2} \overline{F^c} F + h.c. \end{aligned} \tag{1}$$

where $\tilde{\eta} = i\sigma_2 \eta^*$. The first Yukawa term $Y^{\alpha\beta}$ is the Standard Model interaction for leptons, which we can assume to be diagonal in flavor (Greek indices stand for family indices).

2.1 Scalar sector

The scalar potential $\mathcal{V}$ invariant under the $SU(2)\times U(1)\times \mathbb{Z}_2$ symmetry is

$$\begin{aligned}\mathcal{V} = & -m_\phi^2 \phi^\dagger \phi + m_\eta^2 \eta^\dagger \eta - \frac{m_\Omega^2}{2} \mathrm{Tr}(\Omega^\dagger \Omega) \\ & + \frac{\lambda_1}{2} (\phi^\dagger \phi)^2 + \frac{\lambda_2}{2} (\eta^\dagger \eta)^2 + \frac{\lambda_3}{2} (\phi^\dagger \phi)(\eta^\dagger \eta)\end{aligned}$$

$$
\begin{aligned}
&+\lambda_4(\phi^\dagger\eta)(\eta^\dagger\phi)+\frac{\lambda_5}{2}[(\phi^\dagger\eta)^2+(\eta^\dagger\phi)^2]\\
&+\mu_1\phi^\dagger\Omega\phi+\mu_2\eta^\dagger\Omega\eta\\
&+\frac{\lambda_1^\Omega}{2}(\phi^\dagger\phi)\mathrm{Tr}(\Omega^\dagger\Omega)+\frac{\lambda_2^\Omega}{4}[\mathrm{Tr}(\Omega^\dagger\Omega)]^2\\
&+\frac{\lambda_\eta^\Omega}{2}(\eta^\dagger\eta)\mathrm{Tr}(\Omega^\dagger\Omega),
\end{aligned}
\tag{2}
$$

where we make the conservative assumption that m_ϕ^2, m_η^2 and m_Ω^2 are all positive, so that the spontaneous electroweak symmetry breaking will be driven by ϕ and (sub-dominantly) by the neutral component of Ω, while η cannot acquire a VEV. Notice that we are using the standard 2×2 matrix notation for the $\mathrm{SU(2)_L}$ triplets:

$$
\Sigma=\begin{pmatrix}\frac{\Sigma^0}{\sqrt{2}} & \Sigma^+\\ \Sigma^- & -\frac{\Sigma^0}{\sqrt{2}}\end{pmatrix},\quad \Omega=\begin{pmatrix}\frac{\Omega^0}{\sqrt{2}} & \Omega^+\\ \Omega^- & -\frac{\Omega^0}{\sqrt{2}}\end{pmatrix}. \tag{3}
$$

The other couplings appearing in Eq. (2) are constrained by a number of theoretical considerations. First, they must comply with the condition that the potential is bounded from below in order to have a stable minimum. This requirement leads to the following conditions [11,12]

$$
\lambda_1\geq 0,\quad \lambda_2\geq 0,\quad \lambda_2^\Omega\geq 0, \tag{4}
$$

$$
\lambda_3+\sqrt{\lambda_1\lambda_2}\geq 0,\quad \lambda_3+\lambda_4-|\lambda_5|+\sqrt{\lambda_1\lambda_2}\geq 0, \tag{5}
$$

$$
\lambda_1^\Omega+\sqrt{2\lambda_1\lambda_2^\Omega}\geq 0,\quad \lambda_\eta^\Omega+\sqrt{2\lambda_2\lambda_2^\Omega}\geq 0, \tag{6}
$$

$$
\begin{aligned}
&\sqrt{2\lambda_1\lambda_2\lambda_2^\Omega}+\lambda_3\sqrt{2\lambda_2^\Omega}+\lambda_1^\Omega\sqrt{\lambda_2}+\lambda_\eta^\Omega\sqrt{\lambda_1}\\
&+\sqrt{\left(\lambda_3+\sqrt{\lambda_1\lambda_2}\right)\left(\lambda_1^\Omega+2\sqrt{\lambda_1\lambda_2^\Omega}\right)\left(\lambda_\eta^\Omega+\sqrt{\lambda_2\lambda_2^\Omega}\right)}\geq 0.
\end{aligned}
\tag{7}
$$

It is worth noticing that while these conditions ensure that $\mathcal{V}$ is consistently bounded from below at the electroweak scale, the running of the RGEs may lead to breaking of the $\mathbb{Z}_2$ symmetry at some higher energy scale. Another theory restriction comes from the requirement that the expansion of the potential $\mathcal{V}$ around its minimum must be perturbatively valid. In order to ensure this we require that the scalar quartic couplings in Eq. (2) are $\lesssim 1$.

As mentioned before, η does not acquire a VEV and therefore the symmetry breaking is driven only by ϕ and Ω, which have non-zero VEVs:

$$
\langle\phi^0\rangle=v_\phi,\quad \langle\Omega^0\rangle=v_\Omega \tag{8}
$$

The fields η, ϕ and Ω are written as follows

$$
\begin{aligned}
&\eta=\begin{pmatrix}\eta^+\\ (\eta_R+i\eta_I)/\sqrt{2}\end{pmatrix},\quad \phi=\begin{pmatrix}\varphi^+\\ (h_0+v_\phi+i\psi)/\sqrt{2}\end{pmatrix},\\
&\Omega=\begin{pmatrix}(\Omega_0+v_\Omega)/\sqrt{2} & \Omega^+\\ \Omega^- & -(\Omega_0+v_\Omega)/\sqrt{2}\end{pmatrix},
\end{aligned}
\tag{9}
$$

where Ω_0 is real and does not contribute to the CP-odd scalar sector. After symmetry breaking there are three charged scalar fields (only two of which are physical, since one is absorbed by the W boson), plus three CP-even neutral fields, and one physical CP-odd neutral field (since the other is absorbed by the Z boson). The VEVs in Eq. (8) are restricted by the following tadpole equations or minimization conditions

$$
\begin{aligned}
\frac{\partial\mathcal{V}}{\partial\phi}&=v_\phi\left(-m_\phi^2+\frac{1}{2}\lambda_1 v_\phi^2-\frac{\mu_1}{2}v_\Omega+\frac{\lambda_1^\Omega}{4}v_\Omega^2\right)=0,\\
\frac{\partial\mathcal{V}}{\partial\Omega}&=-2m_\Omega^2 v_\Omega+\lambda_2^\Omega v_\Omega^3+v_\phi^2\left(\lambda_1^\Omega v_\Omega-\mu_1\right)=0,
\end{aligned}
\tag{10}
$$

which we solve for m_ϕ^2 and m_Ω^2.

As for the neutral sector, the mass matrix of the CP-even (and $\mathbb{Z}_2$-even) neutral scalars in the basis (ϕ_0,Ω_0) reads

$$
\mathcal{M}_h^2=\begin{pmatrix}\left(-m_\phi^2+\frac{3}{2}\lambda_1 v_\phi^2+v_\Omega\left(-\mu_1+\frac{\lambda_1^\Omega}{4}v_\Omega\right)\right) & \frac{1}{2}v\left(\lambda_1^\Omega v_\Omega-2\mu_1\right)\\ \frac{1}{2}v_\phi\left(\lambda_1^\Omega v_\Omega-2\mu_1\right) & \left(-\frac{1}{2}m_\Omega^2+\frac{3}{4}\lambda_2^\Omega v_\Omega^2+\frac{1}{4}\lambda_1^\Omega v_\phi^2\right)\end{pmatrix}. \tag{11}
$$

The lightest of the neutral scalar mass eigenstates is identified with the SM Higgs boson, h^0 with mass ~ 125 GeV, while the second state, H is a heavier neutral scalar.

On the other hand, the mass matrix for the charged scalars is given as

$$\mathcal{M}^2_{H^\pm} = \begin{pmatrix} \frac{1}{4}\left(2\lambda_1 v_\phi^2 - 4m_\phi^2 + v_\Omega\left(2\mu_1 + \lambda_1^\Omega v_\Omega\right)\right) & \frac{\mu_1 v_\phi}{\sqrt{2}} \\ \frac{\mu_1 v_\phi}{\sqrt{2}} & \frac{1}{2}\left(-2m_\Omega^2 + \lambda_1^\Omega v_\phi^2 + \lambda_2^\Omega v_\Omega^2\right) \end{pmatrix}. \tag{12}$$

Note that, while the Z boson gets its longitudinal component only from the Higgs doublet ϕ and not from the triplet (because Ω^0 is real), the charged Goldstone boson is instead a linear combination of ϕ^+ and Ω^+. The VEV of Ω will then contribute to the W boson mass, thus leading to an upper limit $v_\Omega \lesssim 5$ GeV [23,24]:

$$m_Z^2 = \frac{1}{4}(g^2 + g'^2)v_\phi^2\,,$$
$$m_W^2 = \frac{1}{4}\,g^2(v_\phi^2 + 4\,v_\Omega^2). \tag{13}$$

The mass of the new charged scalar bosons will be

$$m^2_{H^\pm} = \mu_1 \frac{(v_\phi^2 + 2v_\Omega^2)}{2v_\Omega}, \tag{14}$$

$$m^2_{\eta^\pm} = m_\eta^2 + \frac{1}{2}\lambda_3 v_\phi^2 + \frac{1}{\sqrt{2}}\mu_2 v_\Omega + \frac{1}{2}\lambda_\eta^\Omega v_\Omega^2. \tag{15}$$

Because of the conservation of the $\mathbb{Z}_2$ symmetry, the $\mathbb{Z}_2$-odd scalar field η does not mix with any other scalar. It proves convenient to write it in terms of its CP-even and CP-odd components:

$$\eta^0 = \frac{(\eta_R + i\eta_I)}{\sqrt{2}}.$$

The physical masses of the neutral η field are easily determined as

$$m^2_{\eta_R} = m_\eta^2 + \frac{1}{2}(\lambda_3 + \lambda_4 + \lambda_5)v_\phi^2 + \frac{1}{2}\lambda_\eta^\Omega v_\Omega^2 - \frac{1}{\sqrt{2}}\mu_2 v_\Omega, \tag{16}$$

$$m^2_{\eta_I} = m_\eta^2 + \frac{1}{2}(\lambda_3 + \lambda_4 - \lambda_5)v_\phi^2 + \frac{1}{2}\lambda_\eta^\Omega v_\Omega^2 - \frac{1}{\sqrt{2}}\mu_2 v_\Omega. \tag{17}$$

The difference $m^2_{\eta_R} - m^2_{\eta_I}$ depends only on the parameter λ_5 which, as we shall see in the next paragraph, is also responsible for the smallness of neutrino masses. In the limit $\lambda_5 \to 0$ lepton number conservation is restored. Hence, by construction, neutrino masses are "natural", in 't Hooft's sense [25], i.e. they are "symmetry-protected". Moreover, the $\mathbb{Z}_2$ symmetry conservation also makes the lightest of the two eigenstates $\eta_{R,I}$ a viable dark matter candidate, as we will discuss in detail in Sect. 4.

2.2 Fermionic sector

Concerning the fermionic sector, the new triplet scalar Ω allows for a mixing between the singlet and triplet fermion fields – F and Σ – through the Yukawa coupling Y_Ω, as shown in Eq. (1): The mass matrix for the new fermions, in the basis (Σ_0, F) is given as

$$\mathcal{M}_\chi = \begin{pmatrix} M_\Sigma & \frac{1}{\sqrt{2}}Y_\Omega v_\Omega \\ \frac{1}{\sqrt{2}}Y_\Omega v_\Omega & M_F \end{pmatrix}. \tag{18}$$

When the neutral part of Ω acquires a VEV $v_\Omega \neq 0$, the diagonalization of the mass matrix Eq. (18) leads to eigenstates with the following masses (at tree level):

$$m_\chi^\pm = M_\Sigma, \tag{19}$$

$$m_{\chi_1^0} = \frac{1}{2}\left(M_\Sigma + M_F - \sqrt{(M_\Sigma - M_F)^2 + 4(2Y_\Omega v_\Omega)^2}\right), \tag{20}$$

$$m_{\chi_2^0} = \frac{1}{2}\left(M_\Sigma + M_F + \sqrt{(M_\Sigma - M_F)^2 + 4(2Y_\Omega v_\Omega)^2}\right), \tag{21}$$

$$\tan(2\theta) = \frac{4Y_\Omega v_\Omega}{M_\Sigma - M_F}, \tag{22}$$

where θ is the mixing angle between the neutral fermion triplet Σ_0 and F, M_Σ and M_F are the Majorana mass terms for the triplet and the singlet, respectively. Although we will not consider this case here, it is interesting to notice that the lightest neutral eigenstate, χ_1^0 or χ_2^0 may also play the role of the dark matter [9], for more recent analyses see [13,14].

2.3 Neutrino masses

The previous subsection has been dedicated to the spectrum of the new fermions. Let us now comment on neutrino masses. By construction, in the *scotogenic* approach, the dark matter candidate acts as a messenger for neutrino mass generation. Since the $\mathbb{Z}_2$ symmetry is exact, all vertices including new particles must contain an even number of $\mathbb{Z}_2$-odd fields. For this reason neutrinos cannot acquire a tree-level mass term, their masses arising only at the loop level as portrayed in Fig. 1.

The relevant interactions for the generation of neutrino masses arise from Eqs. (1) and (2). The expression for the neutrino mass matrix is [9,11,12]

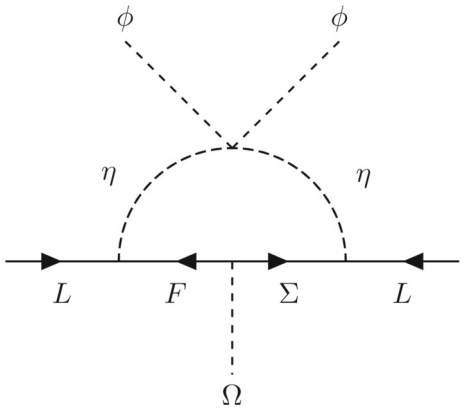

Fig. 1 "Scotogenic" neutrino masses. After electroweak symmetry breaking the SM-like Higgs acquires a VEV $\langle\phi_0\rangle$

$$\begin{aligned}\mathcal{M}^{\nu}_{\alpha\beta} &= \sum_{\sigma=1,2} \frac{Y^{\nu}_{\alpha\sigma} Y^{\nu}_{\beta\sigma}}{32\pi^2} \mathcal{I}_{\sigma}\left(m^2_{\chi_\sigma}, m^2_{\eta_R}, m^2_{\eta_I}\right) \\ &= \sum_{\sigma=1,2} \frac{Y^{\nu}_{\alpha\sigma} Y^{\nu}_{\beta\sigma}}{32\pi^2} m_{\chi_\sigma} \\ &\quad \left(\frac{m^2_{\eta_R}}{m^2_{\eta_R} - m^2_{\chi_\sigma}} \ln\left(\frac{m^2_{\eta_R}}{m^2_{\chi_\sigma}}\right) - \frac{m^2_{\eta_I}}{m^2_{\eta_I} - m^2_{\chi_\sigma}} \ln\left(\frac{m^2_{\eta_I}}{m^2_{\chi_\sigma}}\right)\right),\end{aligned} \tag{23}$$

where α and β are generation indices ($\alpha, \beta = 1, 2, 3$), m_{χ_σ} are the masses of the $\chi^0_{1,2}$ fermion fields and $Y^{\nu}_{\alpha\beta}$ are the new neutrino Yukawa couplings introduced as a 3×2 matrix,[2]

$$Y^{\nu} = \begin{pmatrix} Y^1_{\Sigma} & Y^1_{F} \\ Y^2_{\Sigma} & Y^2_{F} \\ Y^3_{\Sigma} & Y^3_{F} \end{pmatrix} \cdot V(\theta). \tag{24}$$

The matrix $V(\theta)$ is a 2×2 orthogonal matrix that diagonalizes the fermionic mass matrix $\mathcal{M}_{\chi}$ given in Eq. (18). As already noticed before, in the limit $\lambda_5 \to 0$ the two eigenstates m_{η_R} and m_{η_I} are degenerate, hence neutrino masses are zero and the lepton number symmetry is restored. This limit would correspond to an exact cancellation between the η_R and η_I loops. The expression $\mathcal{I}_{\sigma}(m^2_{\chi_\sigma}, m^2_{\eta_R}, m^2_{\eta_I})$ in Eq. (23) involves differences of Passarino–Veltman functions B_0 [26], evaluated in the limit of vanishing external momentum.

We can then rewrite Eq. (23) more compactly as:

$$\mathcal{M}^{\nu}_{\alpha\beta} = Y^{\nu}_{\alpha\beta} v_{\phi} \cdot \frac{\mathcal{F}}{v^2_{\phi}} \cdot Y^{\nu,T}_{\alpha\beta} v_{\phi} \sim m_D \frac{1}{M_R} m^T_D, \tag{25}$$

[2] The new fermions Σ and F match exactly the minimum set needed to describe neutrino oscillations. Indeed, if only one of them is present, the neutrino mass matrix would have only one nonzero eigenvalue, hence unable to account for the solar and atmospheric scales.

where

$$\mathcal{F} = \begin{pmatrix} \frac{\mathcal{I}_1}{32\pi^2} & 0 \\ 0 & \frac{\mathcal{I}_2}{32\pi^2} \end{pmatrix}. \tag{26}$$

This recalls the structure of the standard type-I seesaw neutrino mass relation, with the Dirac mass term given by $Y^{\nu}_{\alpha\beta} v_{\phi}$ and $M^{-1}_R = \frac{\mathcal{F}}{v^2_{\phi}}$ where $\mathcal{F}$ includes the loop functions. In order to compare with the current determination of neutrino oscillation parameters [3], we will apply a Casas–Ibarra parametrization [27]:

$$Y^{\nu}_{\alpha\beta} = U_{\nu} \sqrt{m_{\nu}} \rho \sqrt{\mathcal{F}}^{-1}, \tag{27}$$

where U_{ν} is the lepton mixing matrix, m_{ν} are the neutrino masses (whose squared differences are constrained as in [3]) and the matrix ρ is an arbitrary 2×3 rotation matrix that can be parametrized as [9]

$$\rho = \begin{pmatrix} 0 & \cos(\beta) & \pm\sin(\beta) \\ 0 & -\sin(\beta) & \pm\cos(\beta) \end{pmatrix}. \tag{28}$$

An interesting prediction of this model is that the lightest neutrino is massless. This feature is reminiscent of the "missing partner" nature of this "radiative" seesaw mechanism, in which one of the "right-handed" fermions is missing (there is only one Σ and one F). As a consequence one of the "left" neutrinos can not pair-off and hence remains massless [1].

2.4 Neutrinoless double beta decay

Within the symmetrical parametrisation of the lepton mixing matrix [1] the $0\nu2\beta$ effective mass parameter can be neatly expressed as [28]

$$\begin{aligned}\langle m_{ee}\rangle &= \left|\sum_j U^2_{\nu,ej} m_j\right| \\ &= \left|\cos\theta^2_{12}\cos\theta^2_{13} m_1 + \sin\theta^2_{12}\cos\theta^2_{13} m_2 e^{2i\phi_{12}} \right. \\ &\quad \left. + \sin\theta^2_{13} m_3 e^{2i\phi_{13}}\right|,\end{aligned} \tag{29}$$

where m_i are the three neutrino masses and θ_{1x} are the neutrino mixing angles measured in oscillation experiments. Note that in our case the lightest neutrino is massless ($m_1 = 0$), so that there is only one physical Majorana phase ($\phi \equiv \phi_{12} - \phi_{13}$). Since there is currently no restriction on its value, this phase is a free parameter. Except for this, all other parameters are well measured in oscillation experiments.

We show in Fig. 2 the dependence of $\langle m_{ee}\rangle$ on this phase. One sees that, in contrast to the general case where the three active Majorana neutrinos are massive, here the effective

mass parameter describing the $0\nu2\beta$ decay amplitude has a lower limit [29,30].

The pink (light green) band refers to the 3σ C.L. region allowed by current oscillation experiments [3] for normal (inverted) mass ordering. The black lines correspond to the best fit values for both cases. We also show for comparison the 90% C.L. upper limits (shaded regions) from different experiments: CUORE ($\langle m_{\beta\beta}\rangle < 110-520$ meV) [31], EXO-200 Phase II (147–398 meV) [32], GERDA Phase II (120–260 meV) [33] and KamLAND-Zen (61–165 meV) [34] experiments. The width of these bands is mainly a reflection of the uncertainty in the relevant nuclear matrix elements. The black dashed lines represent the most optimistic future sensitivities for SNO+ Phase II (19–46 meV) [35], LEGEND (15–50 meV) [36] and nEXO after 10 years of data taking (5.7–17.7 meV) [37].

3 Numerical analysis

We now confront the model with current (and future) observations associated both with the primordial cosmological abundance of dark matter, as well as various phenomenological constraints, including the experimental prospects for direct and indirect dark matter detection.

3.1 Parameter scan

We have developed a numerical code using Python, to perform a scan varying randomly the main free parameters which characterize the model. This code is connected to some public computer tools used in particle physics in order to examine the constraints on the model parameters and also quantify the expected sensitivities of future experiments. In particular, our Singlet + Triplet Scotogenic Model is first implemented in `SARAH 4.9.1` [38,39], which calculates all vertices, mass matrices, tadpole equations, one-loop corrections for tadpoles and self-energies. The physical particle spectrum and low-energy observables are computed with `SPheno 4.0.3` [40,41] and `FlavorKit` [42]. In order to perform the dark matter analysis, we use `Micromegas 5.0.2` [43] to compute the thermal component to the dark matter relic abundance as well as the dark matter-nucleon scattering cross sections. For the calculation of the cross sections relevant for the collider analysis, we have used `MadGraph5` [44], importing the UFO files generated with `SARAH 4.9.1`. Our numerical scan was performed with 60,000 points, varying the input parameters as given in Table 2, assuming logarithmic steps. In particular, in the ranges of variation for the values of m_η^2 and $|\lambda_5|$, the lower limits considered were 100 GeV^2 and 10^{-5} respectively, to ensure good behaviour for the $\mathbb{Z}_2$ symmetry [11].

Table 2 Ranges of variation of the input parameters used in the numerical scan

Parameter	Range
M_N	$[5\times10^3, 10^4]$ (GeV)
M_Σ	$[5\times10^3, 10^4]$ (GeV)
m_η^2	[100, 5000] (GeV^2)
$\mu_{1,2}$	$[10^{-8}, 5\times10^3]$ (GeV)
v_Ω	$[10^{-5}, 5]$ (GeV)
$\lvert\lambda_i\rvert, i = 1\ldots4$	$[10^{-8}, 1]$
$\lvert\lambda_5\rvert$	$[10^{-5}, 1]$
$\lvert\lambda_{1,2}^\Omega\rvert$	$[10^{-8}, 1]$
$\lvert\lambda_\eta^\Omega\rvert$	$[10^{-8}, 1]$
$\lvert Y_\Omega\rvert$	$[10^{-8}, 1]$

This model has in principle three potentially viable dark matter candidates: η_R, η_I or χ_0. In the following we will fix $\lambda_5 < 0$ so as to ensure η_R to be the dark matter candidate. This choice is made for definiteness, having in mind that the opposite case with $\lambda_5 > 0$ and η_I as the lightest neutral scalar would also be potentially viable. Notice that the parameters that are not shown in the table are calculated from the ones displayed. For example, m_ϕ^2 and m_Ω^2 are obtained from the tadpole equations (10) and $Y_{\alpha\beta}^\nu$ is calculated via Eq. (27). Note that the smallness of neutrino masses does not preclude these Yukawas from being sizeable, since the neutrino masses are controlled by λ_5 and they are further suppressed by their radiative origin.

3.2 Constraints

The presence of new particles, absent in the Standard Model, will induce departures from the SM predictions for a number of observables. Throughout our analysis, we take into account the following constraints.

a. Theoretical constraints As already discussed in Sect. 2, the coupling and mass parameters appearing in the Lagrangian Eq. (1) are subject to several theoretical constraints. First of all, we must ensure that the scalar potential is bounded from below, which we do by applying the conditions summarised in Eqs. (4). Moreover we must ensure the perturbativity of the couplings, i.e. the scalar quartic couplings are assumed to be $\lesssim \mathcal{O}(1)$. Another theoretical consideration concerns the validity of the $\mathbb{Z}_2$ parity symmetry which is an essential ingredient of this model. Its role is indeed twofold: it stabilises the dark matter candidate η_R and it justifies the one-loop radiative seesaw mechanism which gives mass to neutrinos. Compared to the simple scotogenic model initially proposed in [8], the spontaneous breaking of the $\mathbb{Z}_2$ parity symmetry can be naturally avoided in this extension thanks to the effect on the running of the couplings in the scalar sector

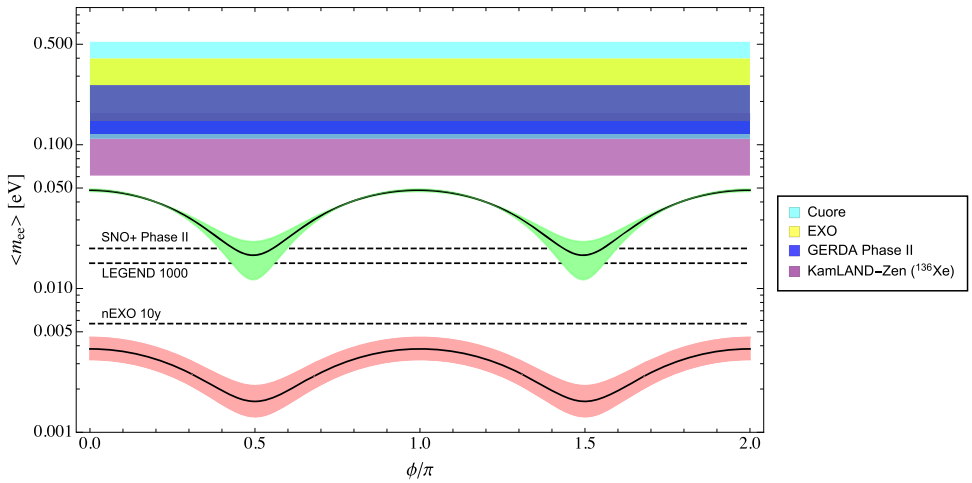

Fig. 2 Effective $0\nu2\beta$ Majorana mass parameter versus the Majorana phase. The pink (light green) band represents the prediction for the 3σ C.L. region allowed by current oscillation experiments for normal (inverted) mass ordering

induced by the inclusion of $\mathbb{Z}_2$-even scalar triplets. Nevertheless, even if the scalar potential is $\mathbb{Z}_2$-preserving at the electroweak scale, the RGEs running could lead to situations where the $\mathbb{Z}_2$ is broken at some higher energy scale [11].[3] While a dedicated analysis of the RGE running is beyond the scope of the present work, we have not ignored this restriction. Following the prescriptions in [11] we have avoided this problem by fixing the ranges of variation of the relevant parameters (m_η^2, μ_2 and v_Ω) so that the $\mathbb{Z}_2$ parity symmetry holds up to higher energies.[4] Moreover, we have checked numerically that, for benchmarks we chose for the collider study in Sect. 5 m_η^2 remains positive at all energy scales. Finally, although experimental constraints place no upper limit on the mass of the heavy neutral scalar H, we require that its decay width should comply with the perturbative unitarity condition, i.e. $\frac{\Gamma_H}{m_H} < \frac{1}{2}$.

b. Neutrino oscillation parameters One of the main motivation of our scotogenic model is to provide an explanation to the generation of neutrino masses. To ensure this, throughout our analysis we require compatibility with the best-fit ranges of the neutrino oscillation parameters. This is enforced via Eq. (27), where the mixing angles and squared mass differences are fixed according to Ref. [3]. For simplicity, the yet unknown Dirac and Majorana phases in U_ν are set to zero. We further assume the currently preferred normal ordering of the light neutrino masses. Interestingly, as already mentioned, this model predicts the lightest active neutrino to be massless.

c. Lepton flavour violation This model could be in principle probed through the observation of charged lepton flavour violation, for example, at high intensity muon facilities [47]. However, the negative results of charged lepton flavor violation searches can be used to set constraints on the parameters of the model, in particular on λ_5 which controls the magnitude of the Yukawa couplings. We apply the most stringent limits to date on the branching fraction of some of such rare processes, namely $\mathrm{BR}(\mu \to e\gamma) < 4.2 \times 10^{-13}$ [48], $\mathrm{BR}(\mu \to eee) < 1. \times 10^{-12}$ [49], $\mathrm{CR}(\mu^-, \mathrm{Au} \to e^-, \mathrm{Au}) < 7 \times 10^{-13}$ [50].

d. Electroweak precision tests The presence of new physics will affect the gauge boson self-energies, parameterised by the oblique parameters [51]. The most important constraint is expected from the T parameter, which is sensitive to the mass splitting between the neutral and charged components of the scalar fields. From the one-loop contribution to the T parameter it follows that $m_{\eta^\pm} - m_{\eta_R} \lesssim 140$ GeV [52]. Given the perturbativity constraint on the relevant λ_i parameters, this condition is automatically fulfilled in all phenomenologically viable solutions of our numerical scan. We require consistency with electroweak precision data by requiring $v_\Omega \lesssim 5$ GeV, in order to get an adequately small deviation of the ρ parameter from one [11] (and consequently a negligible tree level contribution from the triplet to the T parameter), namely we impose $-0.00018 \lesssim \delta\rho \lesssim 0.00096$ (3σ). Moreover, we fix the Higgs VEV v_ϕ in order to get the correct mass of the W boson, inside its experimental range.

e. Invisible decay widths of the Higgs boson If the new neutral scalar masses $m_{\eta_{R,I}}$ are small enough, there can appear new invisible decay channels – at tree level – of the Higgs boson into the lighter stable particles. In the region of parameters where these new invisible decays are possible we enforce that $\mathrm{BR}(h^0 \to \mathrm{inv}) \lesssim 24\%$ [53]. At the loop level, the decay of the Higgs boson into two photons may also be modified by its coupling to the charged scalars. We require consistency at the 3σ level, that is $0.62 \lesssim \mathrm{BR}(h^0 \to \gamma\gamma)/\mathrm{BR}(h^0 \to \gamma\gamma)_{\mathrm{SM}} \lesssim 1.7$.

[3] In addition, finite-temperature corrections to the effective scalar potential may affect the stability of dark matter [45,46].

[4] Notice that requiring the validity of the $\mathbb{Z}_2$ parity symmetry might be over-restrictive. Indeed, UV-completions might contain new degrees of freedom – irrelevant for our phenomenological study – at high energies that could prevent the dangerous breaking.

f. Dipole moments of leptons At the one-loop level the charged scalars present in our model may also induce sizeable contributions to the magnetic dipole moments of leptons. We have required that the contributions to the anomalous muon magnetic dipole moment induced by the new physics do not exceed the allowed discrepancy between the measured value and the one predicted within the SM [53], $\Delta(a_\mu) = a_\mu^{\rm exp} - a_\mu^{\rm SM} = 268(63)(43) \times 10^{-11}$. Contributions to the electric dipole moments arise instead only at the two-loop level, so they are suppressed [52].

g. Dark matter and cosmological observations In the following, we assume a standard cosmological scenario, where the dark matter candidate, the scalar η_R, was in thermal equilibrium with the SM particles in the early Universe. If η_R is the only candidate contributing to the cosmological dark matter, its relic density must comply with the cosmological limits for cold dark matter derived by the Planck satellite data [54,55]: $0.1126 \leq \Omega_{\eta_R} h^2 \leq 0.1246$ (3σ range). Values of $\Omega_{\eta_R} h^2 \leq 0.1126$ are also allowed, if η_R is a subdominant component of the cosmological dark matter and allowing for the existence of another candidate. Moreover, our scenario can be tested at direct detection (DD) experiments, which are meant to probe the nuclear recoil in the scattering of galactic η_R off-nuclei inside the detector. We apply the current most stringent limit on WIMP-nucleon spin-independent (SI) elastic scattering cross section, which has been set by the XENON1T experiment at LNGS [56].

h. Colliders Existing searches for new charged particles at colliders such as LEP and LHC, already set lower limits on their masses in the region below 100 GeV or so [53]. In our analysis we apply the following limits: $m_{H^\pm} \geq 80\,\text{GeV}$ and $122\,\text{GeV} \leq m_{h^0} \leq 128\,\text{GeV}$, the latter to take into account numerical uncertainties.

4 Phenomenology of scalar scotogenic dark matter

In this section we collect the results of our analysis of dark matter in the Triplet + Singlet Scotogenic Model. As already commented before, this model can harbor either fermionic or bosonic WIMP dark matter. Detailed studies of the phenomenology of the fermionic dark matter candidate χ^0 [9] have been presented in Refs. [13,14]. Here we will assume the $\mathbb{Z}_2$-odd scalar η_R to be the dark matter candidate and investigate its phenomenology. The latter has common features with those of the simplest scotogenic constructions [8] as well as the Inert Higgs Doublet Model [18,19,57].

4.1 Relic density

We show in Fig. 3 the expected dark matter relic abundance as a function of the mass of the scalar dark matter candidate

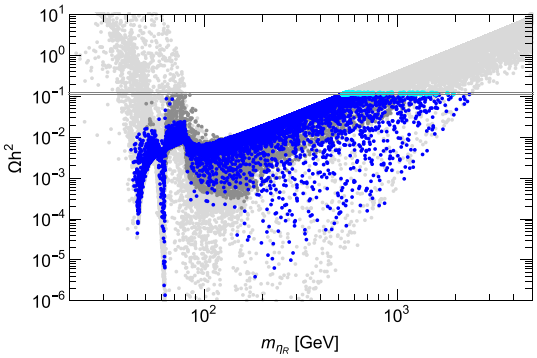

Fig. 3 Relic abundance $\Omega_{\eta_R} h^2$ as a function of the η_R mass. Blue points denote solutions with viable relic density, although leading to underabundant dark matter. Cyan points fall within the 3σ C.L. cold dark matter measurement by the Planck collaboration [54,55]. Grey dots are excluded by at least one of the bounds in Sect. 3.2. Dark grey points are in conflict with the current limit on WIMP-nucleon SI elastic scattering cross section set by XENON1T [56]

η_R. The narrow black band depicts the 3σ range for cold dark matter derived by the Planck satellite data [54,55]. Only for solutions falling exactly in this band (cyan points) the totality of dark matter can be explained by η_R. Blue points refer to solutions where η_R would be subdominant, and another dark matter candidate would be required. Grey points are instead excluded by any of the constraints discussed in Sect. 3.2, mainly by the Planck constraint itself. Dark grey points are solutions in conflict with the current limit on WIMP-nucleon SI elastic scattering cross section set by XENON1T [56]. The features appearing in the plot can be explained by looking in detail into the η_R annihilation channels. The first dip on the left depicts the Z-pole, that is where $m_{\eta_R} \sim M_Z/2$ and the coannihilation via s-channel Z exchange becomes relevant. Similarly, the second depletion of the relic density around $m_{\eta_R} \sim 60$ GeV corresponds to efficient annihilations via s-channel Higgs exchange. Notice that it is likely for solutions in this dip to be in conflict with current collider limits on $\text{BR}(h^0 \to \text{inv})$. The latter depletion is more efficient than the Z-mediated one, which is momentum suppressed. For heavier η_R masses, quartic interactions with gauge bosons become effective and, when kinematically allowed, also two-top final states. Annihilations of η_R into W^+W^- via quartic couplings are particular important at $m_{\eta_R} \gtrsim 80$ GeV thus explaining the third drop in the relic abundance. Finally, in the range $m_{\eta_R} \gtrsim 120$ GeV η_R can annihilate also into two Higgs bosons. At even heavier m_{η_R} the annihilation cross section drops as $\sim \frac{1}{m_{\eta_R}^2}$ and the relic density increases proportionally. Eventually, heavy η_R mainly annihilate into W^+W^-, h^0h^0, HH. We collect all the Feynman diagrams contributing to η_R annihilations and co-annihilations in Appendix A. We may also notice that the relic abundance constraint does not put any bound on the absolute value of the $|\lambda_5|$ parameter. On the other hand, coannihilations with η_I and $\eta^\pm$ may occur in

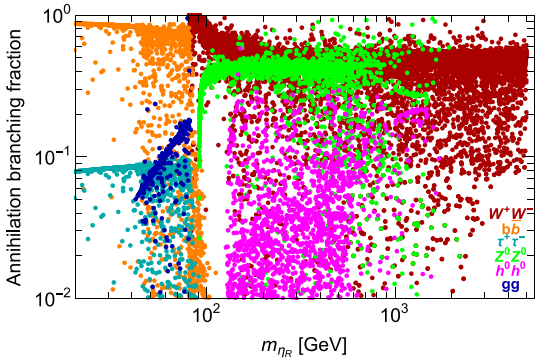

Fig. 4 Main branching fractions of the annihilation cross section of η_R into SM final states versus the mass of η_R. Orange points refer to annihilation into $b\bar{b}$, dark cyan to $\tau^+\tau^-$, blue to gluons, dark red to W^+W^-, green to Z^0Z^0 and magenta to h^0h^0

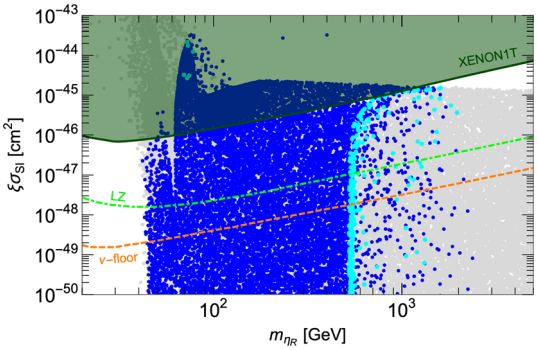

Fig. 5 Spin-independent η_R-nucleon elastic scattering cross section versus the η_R mass. Colour code as in Fig 3. The dark green line denotes the most recent upper bound from XENON1T [56]. The dashed orange line depicts the lower limit corresponding to the "neutrino floor" from coherent elastic neutrino-nucleus scattering (CEνNS) [62], while the green dot-dashed one stands for the projected sensitivity for LZ [63]

all regions of the parameter space with the effect of lowering the relic abundance.

We show in Fig. 4 the most relevant branching ratios (at tree level) for the annihilation cross section of η_R into SM final states versus the mass of η_R, from our numerical scan. Different kinematical regimes are visible from this figure: below M_W, η_R annihilates predominantly into $b\bar{b}$, gluons or $\tau^+\tau^-$; when the quartic coupling with W becomes kinematically accessible, η_R annihilates mainly into W^+W^-. Similarly, annihilations into h^0h^0, HH and Z^0Z^0 become relevant as soon as kinematically open.

4.2 Direct detection

Let us discuss now the η_R direct detection prospects. The tree-level spin-independent η_R-nucleon interaction cross section is mediated through the Higgs and the Z portals. The relevant Feynman diagrams for this process are summarised in Appendix A. Since the η doublet has nonzero hypercharge, the η_R – nucleon interaction through the Z boson would in general exceed the current constraints from direct detection experiments. Nevertheless, in most of the solutions, λ_5 induces a mass splitting between the CP-odd partner η_I and η_R such that the interaction through the Z boson is kinematically forbidden, or leads to inelastic scattering. The η_R-nucleon interaction via the Higgs is therefore dominant in most of the parameter space. As a consequence, the coupling between η_R and the Higgs boson (which depends on the sum $\lambda_3+\lambda_4+\lambda_5$ and on v_Ω, μ_2 and λ_η^Ω) turns out to be the relevant quantity controlling both this cross section and the signals at LHC that we will discuss in Sect. 5. We show in Fig. 5 the spin-independent η_R-nucleon elastic scattering cross section weighted by $\xi = \frac{\Omega_{\eta_R}}{\Omega_{\text{Planck}}}$ versus the η_R mass. The color code of displayed points is the same as in Fig. 3. The dark green plain line denotes the most recent upper bound from XENON1T [56]. Although we only show the most stringent up-to-date limit from XENON1T, we note that other leading liquid xenon experiments such as LUX [58] and PandaX-II [59] can also probe the spin-independent dark matter-nucleon elastic scattering cross section for dark matter heavier than $\sim$ 50 GeV. On the other hand, DarkSide-50 [60] and DEAP-3600 [61] are less competitive for medium and high-mass WIMPs, because of their higher thresholds and lower exposures.

Finally, we also depict as for comparison the lower limit (dashed orange line) corresponding to the "neutrino floor" from coherent elastic neutrino-nucleus scattering (CEνNS) [62] and the projected sensitivity for LUX-ZEPLIN (LZ, green dot-dashed) [63]. The extended particle content characteristic of the Singlet + Triplet Scotogenic Model in principle allows for a viable scalar dark matter candidate in a wider region of masses, compared to the simplest scotogenic or Inert Higgs Doublet models. Nevertheless, because of current experimental constraints, most of the new allowed solutions with a relic abundance within the 3σ C.L. cold dark matter measurement by the Planck collaboration [54,55] lie in a tight vertical region around $m_{\eta_R} \sim 500-600$ GeV. Lighter η_R lead to viable dark matter, although under-abundant, hence it would then require the existence of an additional dark matter candidate.

Finally, it is worth commenting on how the phenomenology of η_R dark matter compares to that of the scalar dark matter in the simple Scotogenic Model [8]. While the two candidates have similar properties, the presence of a scalar triplet in the Singlet + Triplet Scotogenic Model slightly changes the interaction of η_R with the Higgs boson. As a consequence, both its Higgs-mediated annihilation cross section as well as the η_R-nucleon interaction cross section contain a term dependent on μ_2 and on v_Ω (see the relevant vertex in Appendix B). This is nonetheless weighted by the (small) mixing between h^0 and H. As a result the η_R dark matter

phenomenology turns out to be very similar in both models. The real advantage of the Singlet + Triplet Scotogenic Model comes from the enlarged viable parameter space, especially at low η_R masses, as it avoids the unwanted spontaneous breaking of the $\mathbb{Z}_2$ parity symmetry [11].

4.3 Indirect detection

If η_R annihilates into SM products with a cross section near the thermal relic benchmark value, it may be detected indirectly. Among its annihilation products, γ rays are probably the best messengers since they proceed almost unaffected during their propagation, thus carrying both spectral and spatial information. First we consider prospects of detecting γ rays from η_R annihilations by considering the continuum spectrum up to the η_R mass which originates from decays of the annihilation products. We consider annihilations into $b\bar{b}$, $\tau^+\tau^-$ and W^+W^- to compare with current limits set by the Fermi Large Area Telescope (LAT) satellite [64] and HESS telescope [65]. We show in Fig. 6 the results of our numerical scan of the annihilation cross section (weighted by ξ^2 and by the correspondent branching ratio) versus the η_R mass, for η_R annihilating into $b\bar{b}$ (orange points), $\tau^+\tau^-$ (dark cyan) and W^+W^- (dark red). Grey points are excluded by any of the constraints listed in Sect. 3.2. Points in light red are solutions with relic abundance falling exactly within the 3σ band measured by Planck. In the same figure we also show the 95% C.L. upper limits currently set by the Fermi-LAT with γ-ray observations of Milky Way dwarf spheroidal satellite galaxies (dSphs) based on 6 years of data processed with the Pass 8 event-level analysis [64] (plain lines assuming annihilation into $b\bar{b}$ (orange), $\tau^+\tau^-$ (dark cyan) and W^+W^- (dark red)). Moreover we show as a red dot-dashed curve the current upper limit obtained by H.E.S.S. using Galactic Center (GC) γ-ray data accumulated over 10 years [65], assuming a W^+W^- channel and an Einasto dark matter density profile. Finally, we also depict sensitivity projections for Fermi-LAT from a stacked analysis of 60 dSphs and 15 years of data, in the $b\bar{b}$ channel [66] (dashed orange) and for CTA, for the Milky way galactic halo target, W^+W^- channel and an Einasto dark matter density profile [67]. Although current limits lie a couple of orders of magnitude above the predicted signals in this model, future data from Fermi-LAT and CTA offer promising prospects, eventually allowing one to test part of the parameter space both in the low ($\sim$ 70 GeV) as well as in the high ($\gtrsim$ 500 GeV) mass regions.[5]

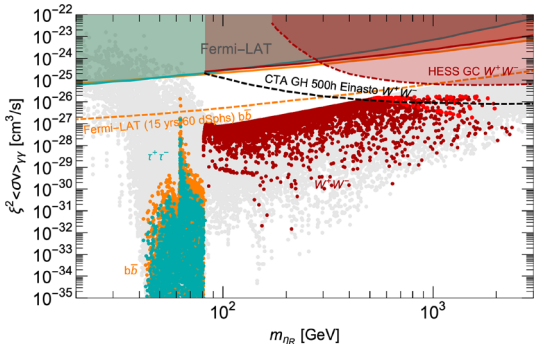

Fig. 6 Predicted η_R annihilation cross section into γ rays – weighted by the relative abundance – for annihilations to $b\bar{b}$ (orange), $\tau^+\tau^-$ (dark cyan) and W^+W^- (dark and light red) final states. The orange, dark cyan and dark red plain lines refer to the corresponding 95% C.L. upper limits currently set by the Fermi-LAT with γ-ray observations of dSphs [64]. The dark red dot-dashed curve is the current upper limit obtained by H.E.S.S. using GC data [65]. We also compare with sensitivity projections for Fermi-LAT ($b\bar{b}$, 60 dSphs and 15 years of data) [66] and for CTA (GC, W^+W^-) [67]. See text for more details

Besides γ rays, charged cosmic rays can be used to probe η_R as a dark matter candidate. The positron fraction measured by PAMELA [73,74] and more recently by AMS-02 [75,76], allows us to place constraints on annihilating WIMPs, which are particularly stringent in the case of annihilations to the first two generations of charged leptons. In our scenario, light η_R annihilate mainly to $\tau^+\tau^-$, as can be seen from Fig. 4. As a result bounds from cosmic positrons are less relevant than those from γ rays. In addition to cosmic-ray positrons, AMS-02 has also provided a high-precision measurement of the cosmic-ray antiproton spectrum [77]. These can be translated into upper limits on hadronic dark matter annihilation, which can be a factor of few stronger than those from γ-ray observations of dSphs [78,79]. Since these results rely on a careful treatment of systematic uncertainties, namely the antiproton production cross-section, and the modelling of the effect of solar modulation we decided not to include them here and leave it for a dedicated work. Similarly, searches for anti-deuterium or anti-helium events could potentially provide a powerful probe of η_R annihilations [80–83], although also affected by substantial uncertainties.

5 Scalar dark matter signatures at the LHC

In this section we confront our scalar dark matter candidate with the latest data from particle colliders, in particular from the LHC run at $\sqrt{s} = 13$ TeV. As in any model with a dark matter candidate, the generic signature to be searched for is missing energy ($\not{E}_T$), measured from the total transverse

[5] Note that for annihilations of non-relativistic η_R occurring at the current epoch, the cross section and hence its indirect detection flux can be affected by a non-perturbative correction, the Sommerfeld enhancement [68–72]. This occurs when $m_{\eta_R} \gg M_W(M_Z)$ and η_R is almost degenerate in mass with $\eta^\pm(\eta_I)$. The multiple exchange of W (Z) bosons would induce a long range attractive force, thus leading to an enhancement of the annihilation cross section at low dark matter velocities, compared to its tree-level value.

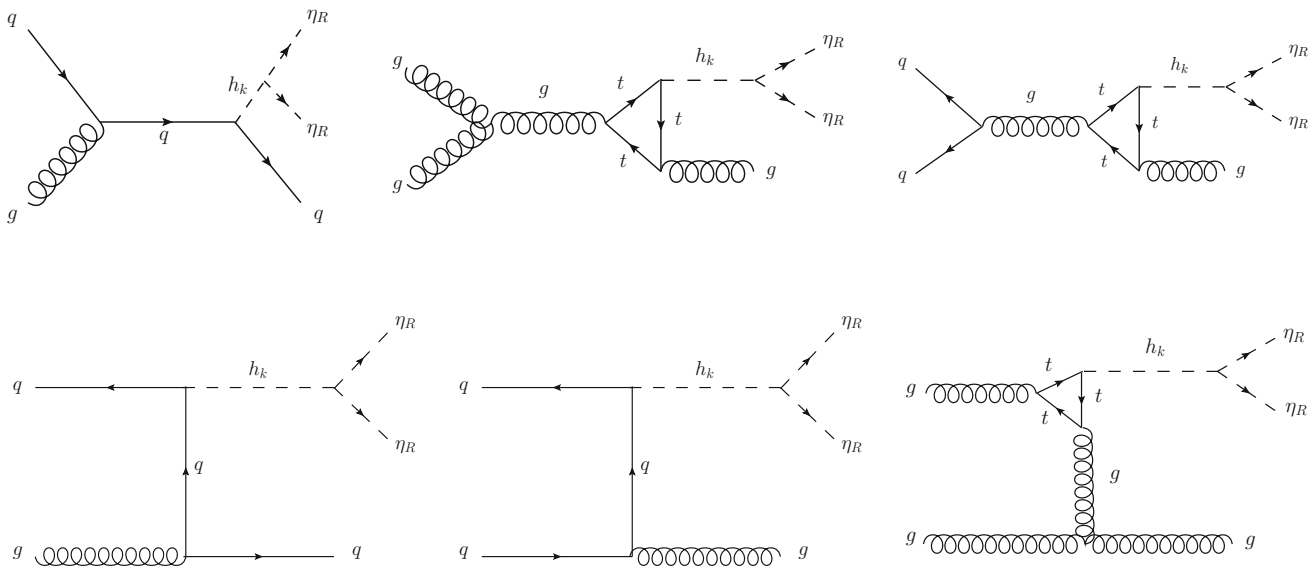

Fig. 7 Relevant Feynman diagrams for mono-jet production through $\eta_R\eta_R + j$ at the LHC; here $h_k \equiv h^0$ or H

momentum recoil of the visible particles in the event (see for instance [84,85]).

In the Triplet + Singlet Scotogenic Model typical signatures are $\not{E}_T + X$, where X can be one or two jets [86,87], two leptons [88] or one photon [89]. Although all of them are in principle interesting, we have checked numerically that in our scenario the most promising one is $\not{E}_T$+ jet (mono-jet). In the following we will focus on mono-jet final states, arising from $pp \to \eta_R\eta_R + g$ and $pp \to \eta_R\eta_R + q$ processes. Here ones looks for events with one high-p_T jet (higher than 100−200 GeV in the central region of the detector, with pseudorapidity $|\eta| < 2.4$) and $\not{E}_T$ above roughly 200 GeV in the 13 TeV analyses for the ATLAS and CMS detectors [86,90]. The dominant irreducible SM background for this channel comes from $Z + j$, with the Z boson subsequently decaying invisibly $Z \to \nu\bar{\nu}$. There is also a subdominant irreducible background from $W + j$, with $W \to \tau\nu$, where the τ decays hadronically. In addition, there are backgrounds from $W + j$ with $W \to \mu\nu$ or $e\nu$, where the lepton is either missed or misidentified as a jet. However, $Z + j$ constitutes approximately 60% of events.

At leading order, the relevant Higgs-mediated Feynman diagrams for mono-jet events are shown in Fig. 7. In all cases, the dark matter is produced via the decay of a neutral scalar (h^0 or H), produced from its interaction with quarks, or through its effective coupling to gluons. The latter involves a top quark loop and enters in gluon-gluon fusion (ggF) processes. An important point is that in ggF processes only the SM-like Higgs doublet couples with fermions. Indeed, since H is mainly a triplet, its coupling with quarks is suppressed. The interaction vertex between η_R and h_k is given in Appendix B. Note that if the mass difference between η_I and η_R is small, η_I should also contribute to the invisible final states. In this case, η_I would subsequently decay to η_R plus soft fermions or jets which are not energetic enough to be detected. Besides Higgs mediation, the mono-jet signal can proceed also via Z-mediation. Therefore we also include the contributions shown in Fig. 8, which are described as $pp \to \eta_R\eta_I + g$ and $pp \to \eta_R\eta_I + q$ processes. Finally, we must mention that in this same scenario of small mass differences, a pair of η_I can also be produced.

5.1 Benchmark points

The constraints previously described in Sect. 3.2 restrict the parameter space allowed by a vast array of experimental probes, among which are the relic density, direct detection and indirect detection analyses. Motivated by these preliminary studies, we now investigate using the `CheckMATE 2` collaboration tools [91–95] whether the solutions that satisfy all experimental limits in Sect. 3.2 could lead to detectable dark matter mono-jet signals at LHC 13 TeV. This code allows us to determine whether or not a given parameter configuration of our model is excluded at 95% C.L, recasting the results of the simulated model in terms of the existing analyses of the LHC, which automatically include the simulation and elimination of the background. Indeed, for each signal region, `CheckMATE 2` computes the expected number of signal events S after cuts, and directly compare it to the 95% C.L. upper limit S^{95}_{exp}, given a signal error ΔS. The most relevant analysis for our study is Ref. [86].

In this way, we identify two interesting benchmark points which survive the entire set of constraints described in Sect. 3.2 (including the theoretical ones, such as the con-

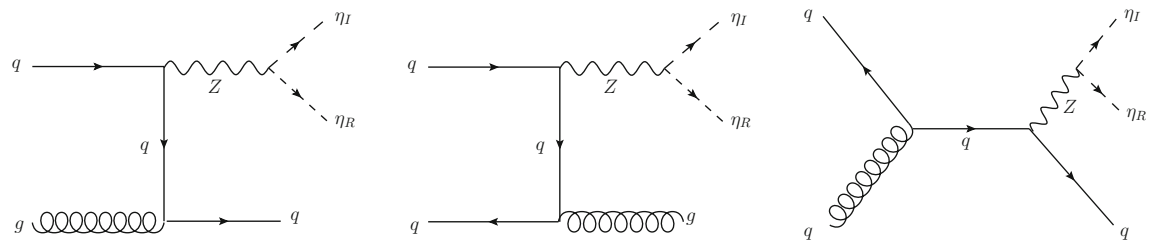

Fig. 8 Feynman diagrams illustrating Z-mediated production of $\eta_R\eta_I + j$ at the LHC

Table 3 Benchmark points which survive the entire set of constraints described in Sect. 3.2 and corresponding parameters relevant to the calculation of diagrams in $\not{E}_T$+jet final states

	Benchmark 1	Benchmark 2	Units
Parameters			
λ_3	3.64×10^{-5}	-1.64×10^{-5}	–
λ_4	7.02×10^{-7}	-3.29×10^{-7}	–
λ_5	-1.8×10^{-2}	-1.45×10^{-2}	–
λ_η^Ω	-1.32×10^{-5}	-7.11×10^{-6}	
μ_2	-4.57×10^{-8}	-1.59×10^{-1}	GeV
v_Ω	2.43×10^{-4}	9.21×10^{-1}	GeV
m_η^2	3678.17	2851.39	GeV^2
Scalar masses			
m_{η_R}	55.92	49.09	GeV
m_{η_I}	65.04	57.38	GeV
m_{h^0}	124.68	125.54	GeV
m_H	425.9	834.45	GeV
Constraints			
Ωh^2	0.0107	0.0129	–
BR($h^0 \to inv.$)	0.155489	0.12939	–
BR($\mu \to e\gamma$)	7.33×10^{-29}	8.55×10^{-32}	–
BR($\mu \to eee$)	3.75×10^{-30}	1.01×10^{-30}	–
CR($\mu^-, Au \to e^-, Au$)	3.88×10^{-29}	1.40×10^{-29}	–
BR($h^0 \to \gamma\gamma$)	0.00226748	0.00212008	–
Δa_μ	2.18×10^{-14}	2.15×10^{-14}	–
σ_{SI}	5.953×10^{-10}	4.862×10^{-10}	pb

servation of the $\mathbb{Z}_2$ parity symmetry up to higher energy scales) and shown in Table 3. Values of the relevant parameters and the corresponding scalar spectrum are summarised. We also show in this table the value of observables obtained in Sect. 3.2 for each benchmark.

The main difference between the two benchmark points is the value of H mass, which is governed by μ_2 and v_Ω.

However, because this heavy scalar is mainly triplet, its coupling with quarks in the ggF processes is suppressed, so that a significant change in its mass is not expected to lead to a large variation in the magnitude of the cross sections.

Table 4 Results obtained with `CheckMATE 2` based on the `atlas_conf_2017_060` [86] analysis by the ATLAS collaboration, for LHC data at $\sqrt{s} = 13$ TeV

Quantity	Benchmark 1	Benchmark 2
$\sigma \pm d\sigma$ [fb]	787.791	1074.62
$S \pm dS$	163.241 ± 6.814	421.3 ± 12.784
r	0.220	0.263

5.2 Mono-jet signatures at the LHC $\sqrt{s} = 13$ TeV

We display in Table 4 the `CheckMATE 2` results for the evaluation in the $\not{E}_T$+jet channel (corresponding to an integrated luminosity of 36.1fb^{-1} in the $\sqrt{s} = 13$ TeV analysis) for the two benchmark points of Table 3. For this study, the cross sections shown in Table 4 correspond to both contributions to the final state studied: Z boson (Fig. 8) and Higgs-mediated processes (Fig. 7), respectively.

The main result of Table 4 is the value of the parameter r

$$r \equiv \frac{S - 1.96\Delta S}{S_{exp}^{95}} \tag{30}$$

calculated by `CheckMATE 2`,[6] which translates into a significant number of signal events after the cuts, S. These specific cuts are implemented by the ATLAS analysis in order to map out the associated regions of consistent parameter choices, and will be described later.

Our dark matter candidate η_R with mass around $\sim$ 50−60 GeV and chosen to satisfy all theoretical and experimental constraints of Sect. 3.2 would lead to a signature in the $\not{E}_T$+jet channel in the ATLAS experiment.

For that we require, for both benchmark points, that the leading jet has $p_T > 250$ GeV and $|\eta| < 2.4$, separation in the azimuthal plane of $\Delta\phi(\text{jet}, p_T^{miss}) > 0.4$ between the

[6] According to algorithm definitions and taking into account experimental errors, a point in parameter space is considered excluded if the ratio $r \geq 1.5$. If $r \leq 0.67$, the point is classified as compatible with the experimental results and is kept. Points with $0.67 < r < 1.5$ are regarded as "potentially excluded" in view of the systematic and theoretical errors. For more details see [96].

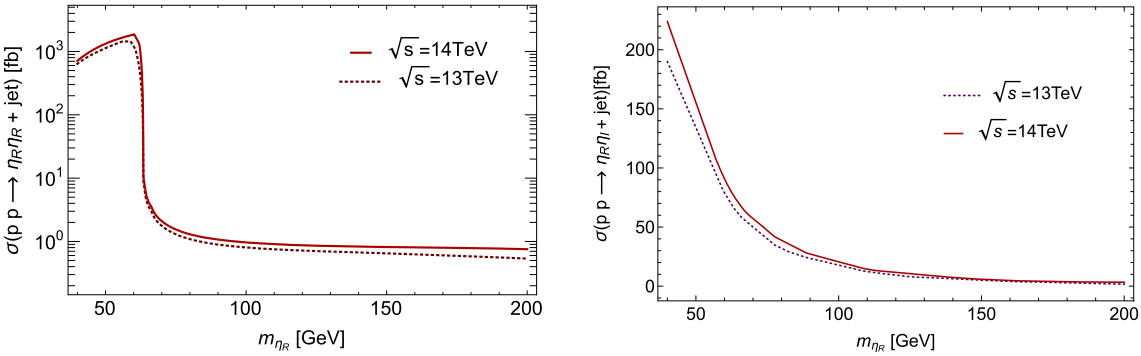

Fig. 9 Cross sections of mono-jet signals at LHC $\sqrt{s} = 13$ (14) TeV. The left panel shows the Higgs boson mediated events from $pp \to \eta_R\eta_R+$ jet. The maximum value of the cross section is $\sim$ 1400(1800) fb for $\sqrt{s} = 13$ (14) TeV respectively. The right panel is the Z-mediated process, $pp \to \eta_R\eta_I+$ jet, with peak contribution $\sim$ 190 (220) fb

missing transverse momentum direction and each selected jet.

The difference between our benchmarks are the $\not{E}_T$ thresholds. While for Benchmark 2 a $\not{E}_T$ minimum of 500 GeV is required, in the other case we take $\not{E}_T >$ 600 GeV.

For larger η_R masses we investigate the behaviour of the cross sections at $\sqrt{s} = 13$ TeV and the projected signal events at $\sqrt{s} = 14$ TeV. We assume the coupling $|\lambda_{345}|$ to lie in the range $[0.02, 0.9]$ and we fix the other parameters according to Benchmark 1 in Table 3. We analyse $\eta_R\eta_R + j$ and $\eta_R\eta_I + j$ separately because the rate of these processes depends on different parameters and we want to analyze their contributions to the total cross section separately.

In Fig. 9 we present the production cross section for $\not{E}_T+$ jet process at LHC $\sqrt{s} = 13$ (14) TeV. Using `Madgraph5` [44] we simulate events with an initial cut of $p_T^{jet} > 100$ GeV, according to the latest analyses in mono-jet searches [97,98]. Since the relevant processes leading to these events are mediated by mainly the SM Higgs (left panel) and Z boson (right panel), one has the characteristic peaks at $m_{\eta_R} \sim m_{h^0}/2$ and at $m_{\eta_R} \sim m_Z/2$ respectively, providing larger cross sections in these mass ranges. Therefore, the Higgs boson mediated processes are dominant up to $m_{\eta_R} \sim 60$ GeV and also contribute in the range $\sim$ [700−1400] fb (13 TeV).

In addition, Z-mediated processes complements the search for $pp \to \eta_R\eta_R+$ jet process at the LHC. For this mass range, the cross sections are $\sim$ [190−80] fb while, for dark matter masses between [65−200] GeV, we have $\sim$ [70−5] fb, providing a sizeable contribution to the total mono-jet cross section, which could be within LHC sensitivity. At $\sqrt{s} = 14$ TeV the cross section increases by a few fb. These results agree with expectations of other models, such as the Inert Higgs Doublet Model, whose contributions to this signal are very similar [97]. In summary, one sees that there are

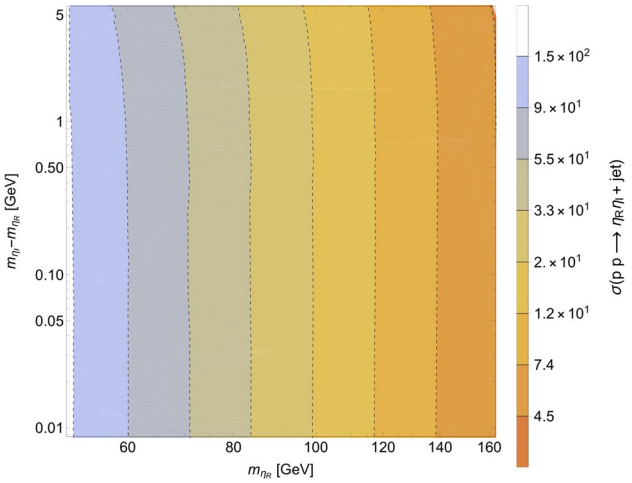

Fig. 10 Mass difference $m_{\eta_I} - m_{\eta_R}$ as a function of m_{η_R} in mono-jet events mediated by the Z boson, $pp \to \eta_R\eta_I+$ jet. The color shades represent values of the cross section in fb

good prospects for probing the mono-jet signal at the LHC for dark matter masses up to $\sim$ 60 GeV.

There are regions of parameters in which η_I and η_R are relatively close in mass, as shown in Fig. 10. This as required for model consistency, as the mass difference between these particles is intimately connected with the smallness of neutrino mass as generated in the scotogenic picture. This requires the violation of lepton number through the value of λ_5, as seen by Eqs. (16) and (17). Indeed, if $m_{\eta_R} - m_{\eta_I}$ is small we can obtain neutrino mass square differences, as needed to account for neutrino oscillation data [4]. Moreover, the particles produced from the decay $\eta_I \to \eta_R$+X are not energetic enough to have the trajectories reconstructed by the detector (soft particles), leading to our $\not{E}_T+$ jet final state signal.

As already commented in previous sections, as a result of its small coupling with quarks, the heavy neutral scalar H does not influence significantly our signal. As shown in

Ref. [12], the production cross section of H at the LHC is 3 to 5 orders of magnitude smaller than the production of the SM Higgs boson, independent of the center-of-mass energy. Hence our results for the scalar dark matter jet + missing energy final states within the Singlet + Triplet Scotogenic Model should also hold within the simplest Scotogenic scenario of [8].

6 Summary and conclusions

In this work we have reexamined the generalized version of the minimal Singlet + Triplet Scotogenic Model, in which dark matter emerges naturally as the mediator of neutrino mass generation and its stability follows from the same $\mathbb{Z}_2$ symmetry also responsible for the radiative origin of neutrino masses. Notice that, while the simplest model of Ma [8] fails to be consistent over a wide range of parameters [10], our generalized scotogenic model is the minimal one allowing for a conserved $\mathbb{Z}_2$ symmetry all the way up to high mass scales [11]. We have assumed dark matter to be a scalar WIMP and we have presented a full numerical analysis of the signatures expected at dark matter detectors as well as collider experiments. We have shown that direct detection data from XENON-1T already disfavour part of the parameter space, in particular solutions with mass in the $\sim$ 100 GeV range. We have highlighted the importance of complementary searches, for instance via indirect detection with γ rays. Although current limits from Fermi-LAT and HESS lie a couple of orders of magnitude above the predicted signals in this model, future sensitivities also for CTA offer promising prospects, eventually allowing to probe both the low and the high WIMP mass regions. We have identified the regions of parameters where dark matter predictions are in agreement with theoretical and experimental constraints, such as those coming from neutrino oscillation data, Higgs data, dark matter relic abundance and direct detection searches. We have also presented expectations for near future direct and indirect detection experiments. These will further probe the parameter space of our scenario. Finally, we have examined the collider signatures associated to the mono-jet channel at the LHC. In particular, we have found a viable light dark matter mass range in the region 50−60 GeV. This should encourage future studies at the upcoming high-luminosity run of the LHC.

Acknowledgements We are deeply grateful to Martin Hirsch and Avelino Vicente for valuable discussions and help with SARAH and SPheno. We also thank Nicolas Rojas and Sebastian Urrutia for their help with the Python numerical code. We further acknowledge useful discussions on ATLAS searches with María Moreno and Florencia Castillo. VDR is also grateful for the kind hospitality received at Fermilab during the final stage of this work. Work supported by the Spanish grants FPA2017-85216-P, SEV-2014-0398 (MINECO/AEI/FEDER, UE), PROMETEO/2018/165 (Generalitat Valenciana) and FPA2017-90566-REDC (Red Consolider MultiDark). IMA thanks the financial support by ANID, Doctorado Nacional (2015) N. 21151255. VDR acknowledges financial support by the "Juan de la Cierva Incorporación" program (IJCI-2016-27736) of the Spanish MINECO and partial support by the EU Horizon 2020 project InvisiblesPlus (690575-InvisiblesPlus-H2020-MSCA-RISE-2015). LCD thanks "Coordenação de Aperfeiçoamento de Pessoal de Nível Superior-Brasil" (CAPES - Finance Code 001) for the financial support.

Data Availability Statement This manuscript has no associated data or the data will not be deposited. [Authors' comment: All relevant data are contained in the article, no additional information is available.]

Open Access This article is licensed under a Creative Commons Attribution 4.0 International License, which permits use, sharing, adaptation, distribution and reproduction in any medium or format, as long as you give appropriate credit to the original author(s) and the source, provide a link to the Creative Commons licence, and indicate if changes were made. The images or other third party material in this article are included in the article's Creative Commons licence, unless indicated otherwise in a credit line to the material. If material is not included in the article's Creative Commons licence and your intended use is not permitted by statutory regulation or exceeds the permitted use, you will need to obtain permission directly from the copyright holder. To view a copy of this licence, visit http://creativecommons.org/licenses/by/4.0/.
Funded by SCOAP[3].

Appendix A: Feynman diagrams for relic abundance and direct detection searches

Here we present some of the main Feynman diagrams relevant to determine the cosmological relic density, assuming that η_R is the dark matter. Fig. 11 shows the main dark matter annihilation and coannihilation channels. Besides the standard s-wave annihilation into quarks and gauge bosons, mediated by the SM-like Higgs boson, coannihilations with both η_R and $\eta^{\pm}$ are possible. These can be mediated either by the Z^0 boson, or also by the new fermions χ_σ. These channels can lead to both charged or neutral leptons in the final state, and involve the contribution of the new Yukawas described in Sect. 2. Notice that these processes are not present in the simplest scotogenic constructions [8] nor in the case of the Inert Higgs Doublet Model [12]. Diagrams with quartic interactions will appear when kinematically allowed, starting at $m_{\eta_R} \gtrsim 80$ GeV.

The diagrams in Fig. 12 contribute to the spin-independent η_R-nucleon elastic scattering cross section at tree level, discussed in Sect. 4.2. The contribution of the diagram on the right is important only when the splitting between the masses of η_R and η_I is small (small λ_5 values) and leads to inelastic signals.

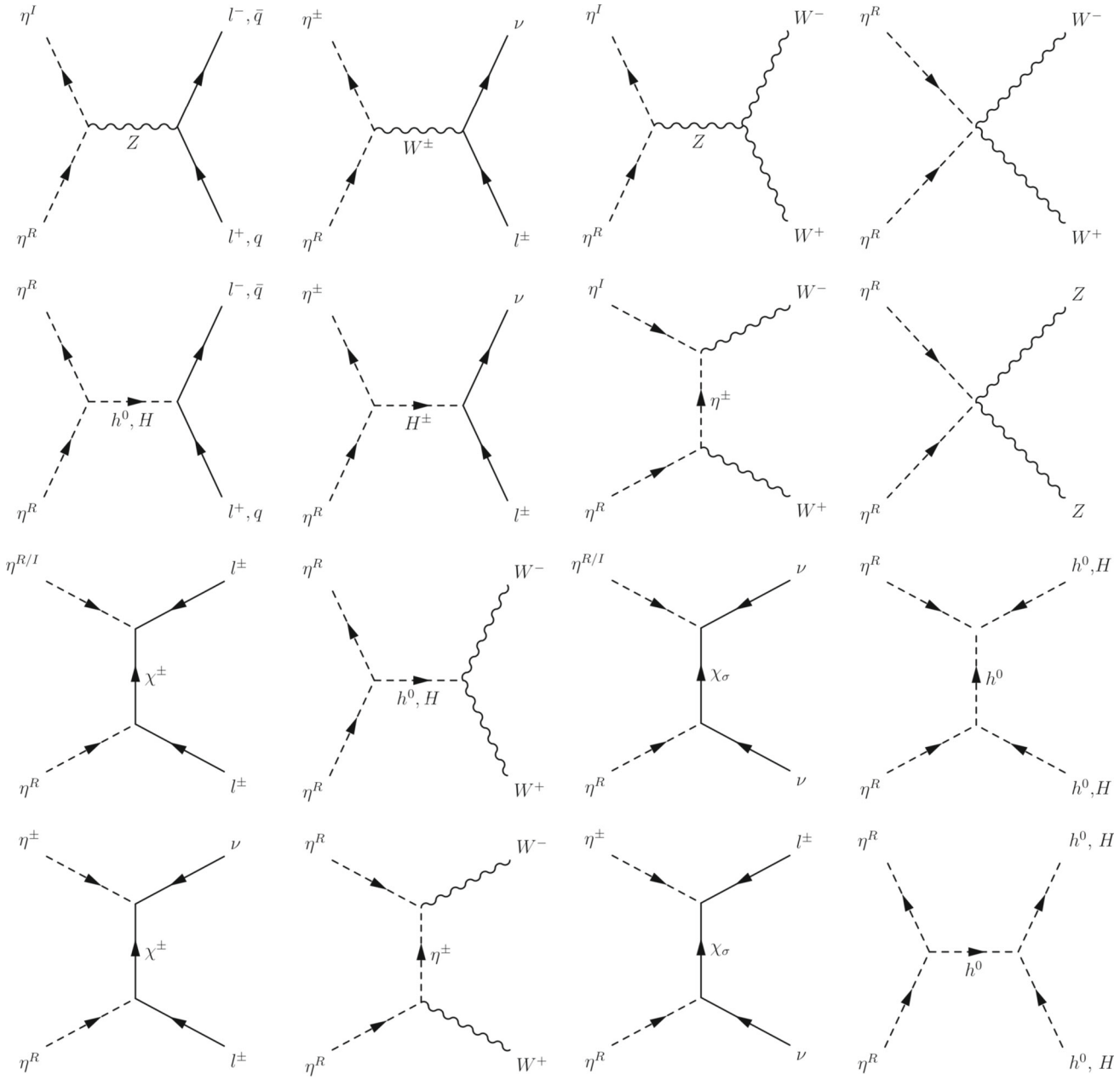

Fig. 11 Relevant annihilation and coannihilation diagrams contributing to the relic abundance of η_R

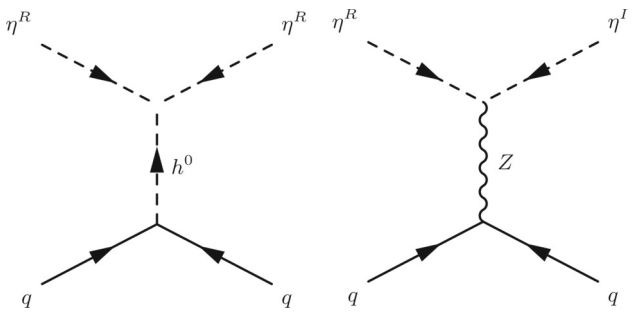

Fig. 12 Tree-level diagrams contributing to the elastic scattering of η_R off nuclei via the Higgs exchange (left) and Z^0-boson exchange (right)

Appendix B: Relevant Feynman rules for the Singlet + Triplet Scotogenic Model

Figure 13 shows the most important Feynman rules for the relevant scalar dark-matter-physics interactions in the Singlet + Triplet Scotogenic Model. These are important for all the signatures studied in this paper, like the η_R-nucleon spin-independent elastic scattering and for the searches in the $\not{E}_T$+jet channel at the LHC.

In contrast to the simplest Scotogenic Model, the interaction vertex with the Higgs is not fully determined by λ_{345},

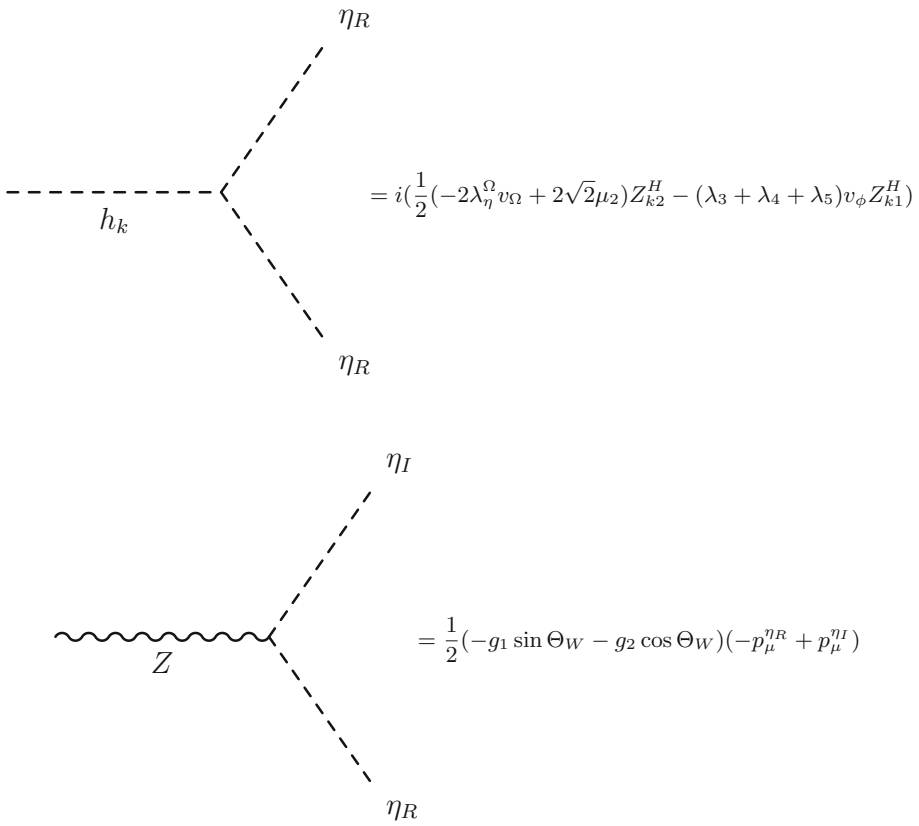

Fig. 13 Relevant η_R interaction vertices. All particle momenta are considered as incoming. In the interaction with neutral scalars, Z_{k1}^H and Z_{k2}^H are entries of the mixing matrix that diagonalizes the mass matrix in Eq. (11) ($k = 1$ refers to the SM Higgs h^0 and $k = 2$ to the heavy scalar H). In the interaction with the Z^0 boson, g_1 and g_2 are the electroweak coupling constants associated to the SM groups $U(1)_Y$ and $SU(2)_L$, respectively

as it contains an extra contribution dependent on λ_η^Ω and μ_2, involving the heavy neutral scalar H, although weighted by its mixing with h^0. Instead, the interaction vertex with the Z^0 boson depends on the quadrimomenta $p_\mu^{\eta_R}$, $p_\mu^{\eta_I}$ and on the electroweak couplings g_1 and g_2.

References

1. J. Schechter, J. Valle, Neutrino masses in SU(2) × U(1) theories. Phys. Rev. D **22**, 2227 (1980). https://doi.org/10.1103/PhysRevD.22.2227
2. N. Rojas, R. Srivastava, J.W. Valle, Simplest Scoto–Seesaw mechanism. Phys. Lett. B **789**, 132–136 (2019). https://doi.org/10.1016/j.physletb.2018.12.014. arXiv:1807.11447 [hep-ph]
3. P. de Salas, D. Forero, C. Ternes, M. Tortola, J. Valle, Status of neutrino oscillations 2018: 3σ hint for normal mass ordering and improved CP sensitivity. Phys. Lett. B **782**(2018), 633–640 (2018). https://doi.org/10.1016/j.physletb.2018.06.019. arXiv:1708.01186 [hep-ph]
4. P. De Salas, S. Gariazzo, O. Mena, C. Ternes, M. Tórtola, Neutrino mass ordering from oscillations and beyond: 2018 status and future prospects. Front. Astron. Space Sci. **5**, 36 (2018). https://doi.org/10.3389/fspas.2018.00036. arXiv:1806.11051 [hep-ph]
5. L. Dorame, D. Meloni, S. Morisi, E. Peinado, J. Valle, Constraining neutrinoless double beta decay. Nucl. Phys. B **861**, 259–270 (2012). https://doi.org/10.1016/j.nuclphysb.2012.04.003. arXiv:1111.5614 [hep-ph]
6. L. Dorame, S. Morisi, E. Peinado, J. Valle, A.D. Rojas, A new neutrino mass sum rule from inverse seesaw. Phys. Rev. D **86**, 056001 (2012). https://doi.org/10.1103/PhysRevD.86.056001. arXiv:1203.0155 [hep-ph]
7. S. King, S. Morisi, E. Peinado, J. Valle, Quark-lepton mass relation in a realistic A_4 extension of the standard model. Phys. Lett. B **724**, 68–72 (2013). https://doi.org/10.1016/j.physletb.2013.05.067. arXiv:1301.7065 [hep-ph]
8. E. Ma, Verifiable radiative seesaw mechanism of neutrino mass and dark matter. Phys. Rev. D **73**, 077301 (2006). https://doi.org/10.1103/PhysRevD.73.077301
9. M. Hirsch, R. Lineros, S. Morisi, J. Palacio, N. Rojas, J. Valle, WIMP dark matter as radiative neutrino mass messenger. JHEP **1310**, 149 (2013). https://doi.org/10.1007/JHEP10(2013)149. arXiv:1307.8134 [hep-ph]
10. A. Merle, M. Platscher, Running of radiative neutrino masses: the scotogenic model—revisited. JHEP **1511**, 148 (2015). https://doi.org/10.1007/JHEP11(2015)148. arXiv:1507.06314 [hep-ph]
11. A. Merle, M. Platscher, N. Rojas, J.W.F. Valle, A. Vicente, Consistency of WIMP Dark Matter as radiative neutrino mass messenger. JHEP **1607**, 013 (2016). https://doi.org/10.1007/JHEP07(2016)013. arXiv:1603.05685 [hep-ph]
12. M.A. Díaz, N. Rojas, S. Urrutia-Quiroga, J.W.F. Valle, Heavy Higgs boson production at colliders in the singlet-triplet scotogenic dark matter model. JHEP **1708**, 017 (2017). https://doi.org/10.1007/JHEP08(2017)017. arXiv:1612.06569 [hep-ph]
13. S. Choubey, S. Khan, M. Mitra, S. Mondal, Singlet-triplet fermionic dark matter and LHC phenomenology. Eur. Phys. J. C **78**, 302 (2018). https://doi.org/10.1140/epjc/s10052-018-5785-1. arXiv:1711.08888 [hep-ph]
14. D. Restrepo, A. Rivera, Phenomenological consistency of the singlet-triplet scotogenic model. JHEP **04**, 134 (2020). https://doi.org/10.1007/JHEP04(2020)134. arXiv:1907.11938 [hep-ph]
15. C. Hagedorn, J. Herrero-García, E. Molinaro, M.A. Schmidt, Phenomenology of the generalised scotogenic model with fermionic dark matter. JHEP **1811**, 103 (2018). https://doi.org/10.1007/JHEP11(2018)103. arXiv:1804.04117 [hep-ph]

16. N.G. Deshpande, E. Ma, Pattern of symmetry breaking with two Higgs doublets. Phys. Rev. D **18**, 2574 (1978). https://doi.org/10.1103/PhysRevD.18.2574
17. R. Barbieri, L.J. Hall, V.S. Rychkov, Improved naturalness with a heavy Higgs: an alternative road to LHC physics. Phys. Rev. D **74**, 015007 (2006). https://doi.org/10.1103/PhysRevD.74.015007
18. M.A. Díaz, B. Koch, S. Urrutia-Quiroga, Constraints to dark matter from inert Higgs doublet model. Adv. High Energy Phys. **2016**, 8278375 (2016). https://doi.org/10.1155/2016/8278375. arXiv:1511.04429 [hep-ph]
19. L. Lopez Honorez, C.E. Yaguna, The inert doublet model of dark matter revisited. JHEP **1009**, 046 (2010). https://doi.org/10.1007/JHEP09(2010)046. arXiv:1003.3125 [hep-ph]
20. L. Lopez Honorez, E. Nezri, J.F. Oliver, M.H. Tytgat, The inert doublet model: an archetype for dark matter. JCAP **0702**, 028 (2007). https://doi.org/10.1088/1475-7516/2007/02/028
21. M. Hirsch, S. Morisi, E. Peinado, J. Valle, Discrete dark matter. Phys. Rev. D **82**, 116003 (2010). https://doi.org/10.1103/PhysRevD.82.116003. arXiv:1007.0871 [hep-ph]
22. M. Boucenna, S. Morisi, E. Peinado, Y. Shimizu, J. Valle, Predictive discrete dark matter model and neutrino oscillations. Phys. Rev. D **86**, 073008 (2012). https://doi.org/10.1103/PhysRevD.86.073008. arXiv:1204.4733 [hep-ph]
23. J. Gunion, R. Vega, J. Wudka, Higgs triplets in the standard model. Phys. Rev. D **42**, 1673–1691 (1990). https://doi.org/10.1103/PhysRevD.42.1673
24. J.F. Gunion, H.E. Haber, G.L. Kane, S. Dawson, The Higgs Hunter's Guide. Front. Phys. **80**, 1–404 (2000)
25. G. 't Hooft, Naturalness, chiral symmetry, and spontaneous chiral symmetry breaking. NATO Sci. Ser. B **59**, 135–157 (1980). https://doi.org/10.1007/978-1-4684-7571-5_9
26. G. Passarino, M. Veltman, One loop corrections for e+ e− annihilation into mu+ mu− in the Weinberg model. Nucl. Phys. B **160**, 151–207 (1979). https://doi.org/10.1016/0550-3213(79)90234-7
27. J. Casas, A. Ibarra, Oscillating neutrinos and muon → e, gamma. Nucl. Phys. B **618**, 171–204 (2001). https://doi.org/10.1016/S0550-3213(01)00475-8
28. W. Rodejohann, J. Valle, Symmetrical parametrizations of the lepton mixing matrix. Phys. Rev. D **84**, 073011 (2011). https://doi.org/10.1103/PhysRevD.84.073011. arXiv:1108.3484 [hep-ph]
29. M. Reig, D. Restrepo, J.F. Valle, O. Zapata, Bound-state dark matter with Majorana neutrinos. Phys. Lett. B **790**, 303–307 (2019). https://doi.org/10.1016/j.physletb.2019.01.023. arXiv:1806.09977 [hep-ph]
30. J. Leite, O. Popov, R. Srivastava, J.W. Valle, A theory for scotogenic dark matter stabilised by residual gauge symmetry. arXiv:1909.06386 [hep-ph]
31. CUORE Collaboration, C. Alduino et al., First results from CUORE: a search for lepton number violation via $0\nu\beta\beta$ decay of ^{130}Te. Phys. Rev. Lett. **120**, 132501 (2018). https://doi.org/10.1103/PhysRevLett.120.132501 arXiv:1710.07988 [nucl-ex]
32. EXO Collaboration, J. Albert et al., Search for neutrinoless double-beta decay with the upgraded EXO-200 detector. Phys. Rev. Lett. **120**, 072701 (2018). https://doi.org/10.1103/PhysRevLett.120.072701. arXiv:1707.08707 [hep-ex]
33. GERDA Collaboration, M. Agostini et al., Improved limit on neutrinoless double-β decay of ^{76}Ge from GERDA phase II. Phys. Rev. Lett. **120**, 132503 (2018). https://doi.org/10.1103/PhysRevLett.120.132503. arXiv:1803.11100 [nucl-ex]
34. KamLAND-Zen Collaboration, A. Gando et al., Search for Majorana neutrinos near the inverted mass hierarchy region with KamLAND-Zen. Phys. Rev. Lett. **117**, 082503 (2016). https://doi.org/10.1103/PhysRevLett.117.109903. arXiv:1605.02889 [hep-ex]
35. SNO+ Collaboration, S. Andringa et al., Current status and future prospects of the SNO+ experiment. Adv. High Energy Phys. **2016**, 6194250 (2016). https://doi.org/10.1155/2016/6194250. arXiv:1508.05759 [physics.ins-det]
36. LEGEND Collaboration, N. Abgrall et al., The large enriched germanium experiment for neutrinoless double beta decay (LEGEND). AIP Conf. Proc. **1894**, 020027 (2017). https://doi.org/10.1063/1.5007652. arXiv:1709.01980 [physics.ins-det]
37. nEXO Collaboration, J. Albert et al., Sensitivity and discovery potential of nEXO to neutrinoless double beta decay. Phys. Rev. C **97**, 065503 (2018). https://doi.org/10.1103/PhysRevC.97.065503. arXiv:1710.05075 [nucl-ex]
38. F. Staub, SARAH 4: a tool for (not only SUSY) model builders. Comput. Phys. Commun. **185**, 1773–1790 (2014). https://doi.org/10.1016/j.cpc.2014.02.018. arXiv:1309.7223 [hep-ph]
39. F. Staub, Exploring new models in all detail with SARAH. Adv. High Energy Phys. **2015**, 840780 (2015). https://doi.org/10.1155/2015/840780. arXiv:1503.04200 [hep-ph]
40. W. Porod, SPheno, a program for calculating supersymmetric spectra, SUSY particle decays and SUSY particle production at e+ e− colliders. Comput. Phys. Commun. **153**, 275–315 (2003). https://doi.org/10.1016/S0010-4655(03)00222-4
41. W. Porod, F. Staub, SPheno 3.1: extensions including flavour, CP-phases and models beyond the MSSM. Comput. Phys. Commun. **183**, 2458–2469 (2012). https://doi.org/10.1016/j.cpc.2012.05.021. arXiv:1104.1573 [hep-ph]
42. W. Porod, F. Staub, A. Vicente, A Flavor Kit for BSM models. Eur. Phys. J. C **74**, 2992 (2014). https://doi.org/10.1140/epjc/s10052-014-2992-2. arXiv:1405.1434 [hep-ph]
43. G. Bélanger, F. Boudjema, A. Pukhov, A. Semenov, micrOMEGAs4.1: two dark matter candidates. Comput. Phys. Commun. **192**, 322–329 (2015). https://doi.org/10.1016/j.cpc.2015.03.003. arXiv:1407.6129 [hep-ph]
44. J. Alwall et al., The automated computation of tree-level and next-to-leading order differential cross sections, and their matching to parton shower simulations. JHEP **1407**, 079 (2014). https://doi.org/10.1007/JHEP07(2014)079. arXiv:1405.0301 [hep-ph]
45. L. Dolan, R. Jackiw, Symmetry behavior at finite temperature. Phys. Rev. D **9**, 3320–3341 (1974). https://doi.org/10.1103/PhysRevD.9.3320
46. M.E. Carrington, Effective potential at finite temperature in the standard model. Phys. Rev. D **45**, 2933–2944 (1992). https://doi.org/10.1103/PhysRevD.45.2933
47. P. Rocha-Moran, A. Vicente, Lepton flavor violation in the singlet-triplet scotogenic model. JHEP **1607**, 078 (2016). https://doi.org/10.1007/JHEP07(2016)078. arXiv:1605.01915 [hep-ph]
48. MEG Collaboration, A. Baldini et al., Search for the lepton flavour violating decay $\mu^+ \to e^+\gamma$ with the full dataset of the MEG experiment. Eur. Phys. J. C **76**, 434 (2016). https://doi.org/10.1140/epjc/s10052-016-4271-x. arXiv:1605.05081 [hep-ex]
49. SINDRUM Collaboration, U. Bellgardt et al., Search for the Decay mu+ —> e+ e+ e−. Nucl. Phys. B **299**, 1–6 (1988). https://doi.org/10.1016/0550-3213(88)90462-2
50. SINDRUM II Collaboration, W.H. Bertl et al., A search for muon to electron conversion in muonic gold. Eur. Phys. J. C **47**, 337–346 (2006). https://doi.org/10.1140/epjc/s2006-02582-x
51. M.E. Peskin, T. Takeuchi, Estimation of oblique electroweak corrections. Phys. Rev. D **46**, 381–409 (1992). https://doi.org/10.1103/PhysRevD.46.381
52. A. Abada, T. Toma, Electric dipole moments in the minimal scotogenic model. JHEP **1804**, 030 (2018). https://doi.org/10.1007/JHEP04(2018)030. arXiv:1802.00007 [hep-ph]
53. Particle Data Group Collaboration, M. Tanabashi et al., Review of particle physics. Phys. Rev. D **98**, 030001 (2018). https://doi.org/10.1103/PhysRevD.98.030001
54. Planck Collaboration, P. Ade et al., Planck 2015 results. XIII. Cosmological parameters. Astron. Astrophys. **594**, A13 (2016). https://

doi.org/10.1051/0004-6361/201525830. arXiv:1502.01589 [astro-ph.CO]
55. Planck Collaboration, N. Aghanim et al., Planck 2018 results. VI. Cosmological parameters. arXiv:1807.06209 [astro-ph.CO]
56. XENON Collaboration, E. Aprile et al., Dark matter search results from a one ton-year exposure of XENON1T. Phys. Rev. Lett. **121**, 111302 (2018). https://doi.org/10.1103/PhysRevLett.121.111302. arXiv:1805.12562 [astro-ph.CO]
57. T. Hambye, F.-S. Ling, L. Lopez Honorez, J. Rocher, Scalar multiplet dark matter. JHEP **0907**, 090 (2009). https://doi.org/10.1088/1126-6708/2009/07/090. arXiv:0903.4010 [hep-ph]
58. LUX Collaboration, D. Akerib et al., Results from a search for dark matter in the complete LUX exposure. Phys. Rev. Lett. **118**, 021303 (2017). https://doi.org/10.1103/PhysRevLett.118.021303. arXiv:1608.07648 [astro-ph.CO]
59. PandaX-II Collaboration, X. Cui et al., Dark matter results from 54-ton-day exposure of PandaX-II experiment. Phys. Rev. Lett. **119**, 181302 (2017). https://doi.org/10.1103/PhysRevLett.119.181302. arXiv:1708.06917 [astro-ph.CO]
60. DarkSide Collaboration, P. Agnes et al., Low-mass dark matter search with the darkside-50 experiment. Phys. Rev. Lett. **121**, 081307 (2018). https://doi.org/10.1103/PhysRevLett.121.081307. arXiv:1802.06994 [astro-ph.HE]
61. DEAP Collaboration, R. Ajaj et al., Search for dark matter with a 231-day exposure of liquid argon using DEAP-3600 at SNOLAB. Phys. Rev. D **100**, 022004 (2019). https://doi.org/10.1103/PhysRevD.100.022004. arXiv:1902.04048 [astro-ph.CO]
62. J. Billard, L. Strigari, E. Figueroa-Feliciano, Implication of neutrino backgrounds on the reach of next generation dark matter direct detection experiments. Phys. Rev. D **89**, 023524 (2014). https://doi.org/10.1103/PhysRevD.89.023524. arXiv:1307.5458 [hep-ph]
63. LUX-ZEPLIN Collaboration, D.S. Akerib et al., Projected WIMP Sensitivity of the LUX-ZEPLIN (LZ) dark matter experiment. arXiv:1802.06039 [astro-ph.IM]
64. Fermi-LAT Collaboration, M. Ackermann et al., Searching for dark matter annihilation from Milky Way dwarf spheroidal galaxies with six years of fermi large area telescope data. Phys. Rev. Lett. **115**, 231301 (2015). https://doi.org/10.1103/PhysRevLett.115.231301. arXiv:1503.02641 [astro-ph.HE]
65. HESS Collaboration, H. Abdallah et al., Search for dark matter annihilations towards the inner Galactic halo from 10 years of observations with H.E.S.S. Phys. Rev. Lett. **117**, 111301 (2016). https://doi.org/10.1103/PhysRevLett.117.111301. arXiv:1607.08142 [astro-ph.HE]
66. Fermi-LAT Collaboration, E. Charles et al., Sensitivity projections for dark matter searches with the fermi large area telescope. Phys. Rep. **636**, 1–46 (2016). https://doi.org/10.1016/j.physrep.2016.05.001. arXiv:1605.02016 [astro-ph.HE]
67. CTA Consortium Collaboration, B. Acharya et al., Science with the Cherenkov Telescope Array (2017). https://doi.org/10.1142/10986. arXiv:1709.07997 [astro-ph.IM]
68. A. Sommerfeld, Über die Beugung und Bremsung der Elektronen. Ann. Phys. **403**, 257–330 (1931). https://doi.org/10.1002/andp.19314030302
69. J. Hisano, S. Matsumoto, M.M. Nojiri, Explosive dark matter annihilation. Phys. Rev. Lett. **92**, 031303 (2004). https://doi.org/10.1103/PhysRevLett.92.031303
70. J. Hisano, S. Matsumoto, M.M. Nojiri, O. Saito, Non-perturbative effect on dark matter annihilation and gamma ray signature from galactic center. Phys. Rev. D **71**, 063528 (2005). https://doi.org/10.1103/PhysRevD.71.063528
71. N. Arkani-Hamed, D.P. Finkbeiner, T.R. Slatyer, N. Weiner, A theory of dark matter. Phys. Rev. D **79**, 015014 (2009). https://doi.org/10.1103/PhysRevD.79.015014. arXiv:0810.0713 [hep-ph]
72. T.A. Chowdhury, S. Nasri, The Sommerfeld enhancement in the scotogenic model with large electroweak scalar multiplets. JCAP **1701**, 041 (2017). https://doi.org/10.1088/1475-7516/2017/01/041. arXiv:1611.06590 [hep-ph]
73. PAMELA Collaboration, O. Adriani et al., An anomalous positron abundance in cosmic rays with energies 1.5–100 GeV. Nature **458**, 607–609 (2009). https://doi.org/10.1038/nature07942. arXiv:0810.4995 [astro-ph]
74. PAMELA Collaboration, O. Adriani et al., Cosmic-ray positron energy spectrum measured by PAMELA. Phys. Rev. Lett. **111**, 081102 (2013). https://doi.org/10.1103/PhysRevLett.111.081102. arXiv:1308.0133 [astro-ph.HE]
75. A.M.S. Collaboration, M. Aguilar et al., First result from the alpha magnetic spectrometer on the international space station: precision measurement of the positron fraction in primary cosmic rays of 0.5–350 GeV. Phys. Rev. Lett. **110**, 141102 (2013). https://doi.org/10.1103/PhysRevLett.110.141102
76. L. Bergstrom, T. Bringmann, I. Cholis, D. Hooper, C. Weniger, New limits on dark matter annihilation from AMS cosmic ray positron data. Phys. Rev. Lett. **111**, 171101 (2013). https://doi.org/10.1103/PhysRevLett.111.171101. arXiv:1306.3983 [astro-ph.HE]
77. A.M.S. Collaboration, M. Aguilar et al., Antiproton flux, antiproton-to-proton flux ratio, and properties of elementary particle fluxes in primary cosmic rays measured with the alpha magnetic spectrometer on the international space station. Phys. Rev. Lett. **117**, 091103 (2016). https://doi.org/10.1103/PhysRevLett.117.091103
78. A. Cuoco, M. Krämer, M. Korsmeier, Novel dark matter constraints from antiprotons in light of AMS-02. Phys. Rev. Lett. **118**, 191102 (2017). https://doi.org/10.1103/PhysRevLett.118.191102. arXiv:1610.03071 [astro-ph.HE]
79. I. Cholis, T. Linden, D. Hooper, A robust excess in the cosmic-ray antiproton spectrum: implications for annihilating dark matter. Phys. Rev. D **99**, 103026 (2019). https://doi.org/10.1103/PhysRevD.99.103026. arXiv:1903.02549 [astro-ph.HE]
80. F. Donato, N. Fornengo, P. Salati, Anti-deuterons as a signature of supersymmetric dark matter. Phys. Rev. D **62**, 043003 (2000). https://doi.org/10.1103/PhysRevD.62.043003
81. E. Carlson, A. Coogan, T. Linden, S. Profumo, A. Ibarra, S. Wild, Antihelium from dark matter. Phys. Rev. D **89**, 076005 (2014). https://doi.org/10.1103/PhysRevD.89.076005. arXiv:1401.2461 [hep-ph]
82. M. Cirelli, N. Fornengo, M. Taoso, A. Vittino, Anti-helium from dark matter annihilations. JHEP **1408**, 009 (2014). https://doi.org/10.1007/JHEP08(2014)009. arXiv:1401.4017 [hep-ph]
83. A. Coogan, S. Profumo, Origin of the tentative AMS antihelium events. Phys. Rev. D **96**(8), 083020 (2017). https://doi.org/10.1103/PhysRevD.96.083020. arXiv:1705.09664 [astro-ph.HE]
84. ATLAS Collaboration, $E_{\mathrm{T}}^{\mathrm{miss}}$ performance in the ATLAS detector using 2015–2016 LHC p-p collisions
85. CMS Collaboration, Performance of missing energy reconstruction in 13 TeV pp collision data using the CMS detector
86. ATLAS Collaboration, M. Aaboud et al., Search for new phenomena in final states with an energetic jet and large missing transverse momentum in pp collisions at $\sqrt{s} = 13$ TeV using the ATLAS detector. Phys. Rev. D **94**, 032005, (2016). https://doi.org/10.1103/PhysRevD.94.032005. arXiv:1604.07773 [hep-ex]
87. U. Haisch, G. Polesello, Searching for dark matter in final states with two jets and missing transverse energy. JHEP **1902**, 128 (2019). https://doi.org/10.1007/JHEP02(2019)128. arXiv:1812.08129 [hep-ph]
88. ATLAS Collaboration, M. Aaboud et al., Search for new phenomena using the invariant mass distribution of same-flavour opposite-sign dilepton pairs in events with missing transverse momentum in $\sqrt{s} = 13$ TeV pp collisions with the ATLAS detector. Eur. Phys. J. C **78**, 625, (2018). https://doi.org/10.1140/epjc/s10052-018-6081-9. arXiv:1805.11381 [hep-ex]

89. ATLAS Collaboration, M. Aaboud et al., Search for dark matter at $\sqrt{s} = 13$ TeV in final states containing an energetic photon and large missing transverse momentum with the ATLAS detector. Eur. Phys. J.C **77**, 393, (2017). https://doi.org/10.1140/epjc/s10052-017-4965-8. arXiv:1704.03848 [hep-ex]
90. Measurements of the Higgs boson production and decay rates and constraints on its couplings from a combined ATLAS and CMS analysis of the LHC pp collision data at $\sqrt{s} = 7$ and 8 TeV
91. D. Dercks, N. Desai, J.S. Kim, K. Rolbiecki, J. Tattersall, T. Weber, CheckMATE 2: from the model to the limit. Comput. Phys. Commun. **221**, 383–418 (2017). https://doi.org/10.1016/j.cpc.2017.08.021. arXiv:1611.09856 [hep-ph]
92. T. Sjostrand, S. Mrenna, P.Z. Skands, A brief introduction to PYTHIA 8.1. Comput. Phys. Commun. **178**, 852–867 (2008). https://doi.org/10.1016/j.cpc.2008.01.036. arXiv:0710.3820 [hep-ph]
93. DELPHES 3 Collaboration, J. de Favereau et al., DELPHES 3, a modular framework for fast simulation of a generic collider experiment. JHEP **1402**, 057 (2014). https://doi.org/10.1007/JHEP02(2014)057. arXiv:1307.6346 [hep-ex]
94. M. Cacciari, G.P. Salam, G. Soyez, FastJet User Manual. Eur. Phys. J. C **72**, 1896 (2012). https://doi.org/10.1140/epjc/s10052-012-1896-2. arXiv:1111.6097 [hep-ph]
95. A.L. Read, Presentation of search results: the CL(s) technique. J. Phys. G **28**, 2693–2704. (2002). https://doi.org/10.1088/0954-3899/28/10/313
96. F. Domingo, J.S. Kim, V. Martin-Lozano, P. Martin-Ramiro, R. Ruiz de Austri, Confronting the neutralino and chargino sector of the NMSSM to the multi-lepton searches at the LHC. arXiv:1812.05186 [hep-ph]
97. A. Belyaev et al., Advancing LHC probes of dark matter from the inert two-Higgs-doublet model with the monojet signal. Phys. Rev. D **99**, 015011 (2019). https://doi.org/10.1103/PhysRevD.99.015011. arXiv:1809.00933 [hep-ph]
98. A. Belyaev, G. Cacciapaglia, I.P. Ivanov, F. Rojas-Abatte, M. Thomas, Anatomy of the inert two Higgs doublet model in the light of the LHC and non-LHC dark matter searches. Phys. Rev. D **97**, 035011 (2018). https://doi.org/10.1103/PhysRevD.97.035011. arXiv:1612.00511 [hep-ph]